On the Direct Correlation between Gamma-Rays and PeV Neutrinos from Blazars

Shan Gao[1], Martin Pohl[1,2], and Walter Winter[1]

[1] Deutsches Elektronen-Synchrotron (DESY), Platanenallee 6, D-15738 Zeuthen, Germany; shan.gao@desy.de
[2] Institute of Physics and Astronomy, University of Potsdam, D-14476 Potsdam, Germany

Abstract

We study the frequently used assumption in multi-messenger astrophysics that the gamma-ray and neutrino fluxes are directly connected because they are assumed to be produced by the same photohadronic production chain. An interesting candidate source for this test is the flat-spectrum radio quasar PKS B1424-418, which recently called attention to a potential correlation between an IceCube PeV neutrino event and its burst phase. We simulate both the multi-waveband photon and the neutrino emission from this source using a self-consistent radiation model. We demonstrate that a simple hadronic model cannot adequately describe the spectral energy distribution for this source, but a lepto-hadronic model with a subdominant hadronic component can reproduce the multi-waveband photon spectrum observed during various activity phases of the blazar. As a conclusion, up to about 0.3 neutrino events may coincide with the burst, which implies that the leptonic contribution dominates in the relevant energy band. We also demonstrate that the time-wise correlation between the neutrino event and burst phase is weak.

Key words: galaxies: jets – gamma rays: general – neutrinos

1. Introduction

The diffuse flux of TeV–PeV neutrinos detected with IceCube indicates extraterrestrial neutrino emission from cosmic accelerators (Aartsen et al. 2013; IceCube Collaboration 2013) of yet unknown nature. Among the prime source candidates are blazars, active galactic nuclei (AGNs) featuring a relativistic jet roughly oriented along the line of sight to the observer. There is a rich literature modeling the neutrino emission from blazars and searching for positional and temporal correlations between the IceCube neutrino events and blazars (see, e.g., Ahlers & Halzen 2014; Dimitrakoudis et al. 2014; Krauß et al. 2014; Diltz & Böttcher 2016; Halzen & Kheirandish 2016; Padovani et al. 2016; Petropoulou et al. 2016; Righi et al. 2017 and references therein), as well as studying diffuse neutrino emission (Dermer et al. 2014; Murase et al. 2014).

Blazars significantly contribute to the diffuse (extragalactic) γ-ray background (Ajello et al. 2015). If these γ-rays originate from proton interactions, the energy budget will be in principle sufficient to account for the intensity of IceCube neutrinos (Murase et al. 2013). However, recent stacking analyses using IceCube data suggest that blazars at most contribute 7%–27% of the observed neutrino intensity (Aartsen et al. 2017). Similar arguments apply to other promising source candidates, such as radio galaxies (Becker Tjus et al. 2014; Hooper 2016), starburst galaxies (Bechtol et al. 2017; Murase et al. 2016), and gamma-ray bursts (Abbasi et al. 2012; Aartsen et al. 2015). Although the origin of the astrophysical neutrinos is still unknown, the known constraints still permit that at least about 10% of the observed neutrinos were produced by blazars (Aartsen et al. 2017), possibly even by a few particularly neutrino-bright blazars.

Blazars typically exhibit a two-hump structure in their spectral energy distribution (SED; Fossati et al. 1998; Ghisellini et al. 2017). This structure has been successfully reproduced by both leptonic and hadronic models for a number of blazars (Böttcher et al. 2013). In a leptonic model, the low-energy and high-energy humps of the SED are produced by the synchrotron emission from electrons and the inverse-Compton

(IC) scatter of soft photons (such as synchrotron photons from the same electrons), respectively. In a hadronic model, the primary electron synchrotron generates the low-energy hump as well, but secondaries from hadronic processes induced by $p\gamma$ interactions are responsible for the γ-ray emission. In the simplest cases, it is frequently assumed that in $p\gamma$ interactions, the energy deposited in neutrinos (from $\pi^{\pm}$ decays) is roughly comparable to that in γ-rays (from π^0 decays), which means that the neutrino and γ-ray fluxes are directly correlated. Note, however, that even in hadronic models, the leading mechanism to generate the second hump may be, for instance, synchrotron radiation of secondary electrons produced by photohadronic interactions. In addition, it may be possible that for certain astrophysical objects, the emission in the second hump must be dominated by processes of purely leptonic origin. The study of this direct correlation is therefore the main motivation of this work.

One interesting test case for the direct neutrino–γ-ray correlation is the flat-spectrum radio quasar (FSRQ) PKS B1424-418. In Kadler et al. (2016, hereafter K16), a positional and temporal coincidence between the 2 PeV neutrino event (IceCube event 35, IC35, or "Big Bird") and a burst of PKS B1424-418 was reported. After analyzing the γ-ray fluences from blazars in the positional-uncertainty region of IC35 as well as the diffuse γ-ray emission, it was concluded that the burst of PKS B1424-418 had sufficient energy to account for the IceCube event, while the probability of a chance coincidence was around 5%. The required neutrino production efficiency was obtained by scaling the measured neutrino output to the γ-ray fluence in the energy range from 5 keV to 10 GeV ($10^{18.1}$–$10^{24.4}$ Hz) and found to be consistent with that theoretically expected on the grounds of flavor, spectral effects, and source-population selection. An important ingredient was the assumption that the SED in that respective energy range was of hadronic origin, implying our direct correlation. We study whether this assumption can be maintained in a self-consistent ansatz. Note that although we focus on one astrophysical object in this study, our conclusions will be

more profound, as this direct correlation is widely used in multi-messenger analyses; see, e.g., Turley et al. (2016).

The hadronic model of blazars typically involve many parameters (Böttcher et al. 2013), even in the simplest case: a parameter set for primary electrons, a set for protons, and a set for the bulk features of the emitting region, such as size (radius), magnetic-field strength, and Doppler factor, since none of these can be robustly derived from first principles or direct observations. The characteristics for the SEDs vary greatly among the blazars (Ghisellini et al. 2017), and therefore the best-fit parameters, even for purely leptonic models, exhibit large variations; an example is the leptonic models of Finke et al. (2008) versus Tavecchio et al. (2013) for PKS B1424-418. Most neutrinos are produced in $p\gamma$ interactions near the $p\gamma$ threshold, and therefore the neutrino yield strongly depends on the density and spectrum of target photons. Even the simple assumption used in many studies, namely, $L_\nu \propto L_\gamma$ (see, e.g., Righi et al. 2017; Aartsen et al. 2017), is questionable, and an accurate and self-consistent calculation of the SED and the neutrino spectrum is necessary. The calculation also needs to be efficient to permit scanning a large parameter space. In this paper, we present such a code and use it together with analytical calculations to explore what kind of model and which model parameters provide a consistent description of both the SED and the rate of PeV neutrinos.

This paper is structured as follows: in Section 2, we introduce the general setup, and we use analytical calculations to determine the kind of model viable for PKS B1424-418; in Section 3, we briefly introduce our numerical methods and we present the results: the quality of the SED fit, the likelihood of having the observed neutrino event, and the corresponding parameters. The implications of the results are discussed in Section 4. The technical details of the analytical calculation, kinetic equations for the simulations, and the numerical treatments are described in Appendices A, B and C, respectively. We use cgs units in the paper, unless specified otherwise.

2. General Analysis and Models

In this section, we broadly list possible models and give generic constraints based on the characteristics of the SED for the source. The conclusions are derived using analytical and semi-analytical methods.

2.1. Assumptions and List of Models

We use a one-zone model consisting of an isotropic, homogeneous, and spherical emission region, or blob, with radius $R'_{\rm blob}$, that moves relativistically with Doppler factor $\Gamma_{\rm bulk}$. Electrons and protons are injected with power-law spectra, $d^2n'/d\gamma'dt' = K'\gamma'^{-\alpha}$ for $\gamma'_{\rm min} < \gamma' < \gamma'_{\rm max}$, where $d^2n'/d\gamma'dt'$ is the differential particle injection rate per volume, α the power-law index, $\gamma'_{\rm min}$ and $\gamma'_{\rm max}$ the minimum and maximum Lorentz factor of the particles, and K' a normalization factor determined by the particle injection luminosity, $L'_{\rm inj}$. The injected electrons are henceforth referred to as primary electrons, whereas we denote as secondary electrons those created by hadronic interactions or $\gamma\gamma$ pair production. We allow primary electrons and protons to have separate parameter values for $L'_{\rm inj}$, $\gamma'_{\rm min}$, $\gamma'_{\rm max}$, and α. The emission region is assumed to be filled with a homogeneous, randomly oriented magnetic field of strength B'. Neutrinos and "optically thin"

photons can freely stream out of the blob on the timescale $t'_{\rm fs} = 3R'/4c$. For simplicity, we assume the escape rate for charged particles, in the slow cooling case, to be a fixed multiple of the free-streaming timescale, $t_{\rm esc} = t_{\rm fs}/f_{\rm esc} = 10\ t_{\rm fs}$.[3]

The list of relevant interactions includes synchrotron emission and synchrotron self-absorption, IC scattering by both electrons and protons, $\gamma\gamma$ pair production and annihilation, Bethe–Heitler (BH) photo-pair production $p + \gamma \to p + e^\pm$, and photohadronic ($p\gamma$) interactions ($X + \gamma \to X' + \pi$), where X and X' denote either a proton or a neutron and π includes charged or neutral pions. Secondary particles such as $\pi^\pm$ and $\mu^\pm$ can in principle radiate before they decay, but for the parameter values relevant to this study, the effect is negligible. The details are listed in Table 4 and described in Appendix B.

The low-frequency hump in the SED of a generic blazar extends from the radio band to the UV, and in some cases even to the X-ray band; the high-frequency component can be observed from X-rays up to TeV γ-rays. Here we discuss four scenarios that may in principle account for the shape of the SED: the pure leptonic (SSC) model, the lepto-hadronic synchrotron-self-Compton (LH-SSC) model, the lepto-hadronic pion (LHπ) model, the lepto-hadronic proton-synchrotron model, and the proton model, which is a purely hadronic model. The defining features of these models are summarized in Table 1.

In both the SSC and LH-SSC models, the first hump is described by synchrotron emission of primary electrons, and the high-frequency component is due to IC scattering of those photons by the same electrons. The LH-SSC model contains an additional hadronic component compared to the pure leptonic SSC model, which may fill the gap between the two humps (e.g., accounting for the X-ray emission from PKS B1424-418).

In the "lepto-hadronic" models internally, the low-frequency hump is likewise described by synchrotron emission of primary electrons, whereas the second hump arises from hadronic processes. Depending on the parameters of the source, the dominant contribution to the second peak can be γ-rays from π^0 decays, synchrotron and IC radiation emitted by $e^\pm$ from $\pi^\pm$ decays, internal $\gamma\gamma$ annihilation, or proton-pair production (BH), where it can be called an "LH-π" model. The second peak can also be produced in some cases by the proton-synchrotron model (e.g., FSRQ 3C 279; Diltz et al. 2015), namely, the "LH-psyn" model.

In the proton model, leptonic emission is subdominant at all wavebands. The first peak in the SED is attributed to proton-synchrotron radiation, and the second peak is produced by the same type of hadronic processes in the LH-π model.

---

[3] This is clearly an oversimplification as the modeling of the particle escape requires a detailed specification of the geometry, the boundary conditions, the magnetic-field configuration, etc. The escape rate itself is likely to be energy dependent on account of energy-dependent diffusion. In fact, the synchrotron emission of escaped electrons may be responsible for the extended emission regions seen in VLBI radio data, and we do include such a component with the corresponding escape rate to fit the radio data in Figure 4. Note that to some degree, the effect of energy-dependent escape can be compensated with an appropriate choice of the other free parameters such as $L'_{e,\rm inj}$ and $\alpha_{e,\rm inj}$. See also Chen et al. (2015, 2016) for blazar models including an explicit treatment of diffusive escape and its effect on the particle density. Another possible scenario is to include an adiabatic cooling term that dominates over the escape rate, and this effect shows up effectively as an energy-independent extinction term in the kinematic equations. One implication is an explicit time dependence of particle densities arising from expansion. Besides, a steady state can be reached only for specific geometries such as a stationary perturbation in an expanding flow, and modeling the SED in this way is beyond the scope of the paper.

Table 1
List of Models

	First Peak (eV–keV)	Middle Range (keV–MeV)	Second Peak (MeV–TeV)
SSC (Pure leptonic)	L Primary e^- synchrotron	L SSC	L SSC
LH-SSC (Lepto-hadronic)	L Primary e^- synchrotron	H Secondary leptonic	L SSC by primary e^-
LH-π (Lepto-hadronic)	L Primary e^- synchrotron	H Secondary leptonic	H Secondary leptonic or γ-rays from direct π^0 decay
LH-psyn (Proton synchrotron)	L Primary e^- synchrotron	H Proton synchrotron or secondary leptonic	H Proton synchrotron
Proton (Pure hadronic)	H Proton synchrotron	H Secondary leptonic	H Secondary leptonic or γ-rays from direct π^0 decay

Note. In the table, "L"—"Leptonic" and "H"—"Hadronic." "LH" is the abbreviation for "Lepto-hadronic," which is a mixture of Leptonic and Hadronic components.
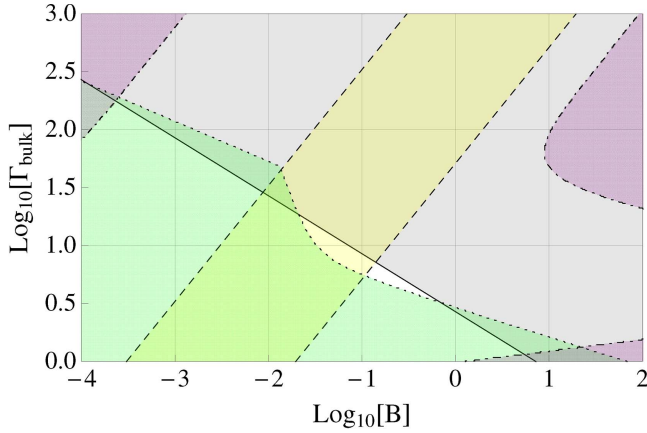
Figure 1. Allowed parameter regions for the LH-π model (cf., Section 2.2). Green: lower-left region with dotted boundary, corresponding to constraint 1; gray: upper-right region delimited by the solid line, constraint 2; yellow area between the dashed parallel lines, constraint 3; purple: the three separate regions formed by dotted–dashed boundaries, constraint 4.

2.2. Constraints on Models and Parameters from Semi-analytical Calculations

While both the leptonic and the hadronic models have successfully explained the SED of a number of blazars, for example Mrk 421, 3C 279, etc., the unique combination of the SED with the PeV neutrino information places stringent limits on the model of PKS B1424-418. Here we use analytical and semi-analytical calculations to demonstrate that neither the lepto-hadronic (LH-π, LH-psyn) nor the purely hadronic proton model can simultaneously explain the SED and the PeV neutrino event, leaving the SSC and LH-SSC models of the SED as the only viable contenders. Analytical arguments also give useful constraints on the parameter space.

Proton model: In pγ interactions, the neutrino energy is roughly 5% that of the parent proton, $E_\nu \sim 0.05\,E_p$. For PKS B1424-418 at the redshift $z = 1.522$, the Lorentz factor of the proton in the comoving frame can be written in terms of the bulk Lorentz factor of the blob Γ and the neutrino energy in the observer frame $E_{\nu,\mathrm{PeV}}^{\mathrm{ob}} \equiv E_\nu^{\mathrm{ob}}/\mathrm{PeV}$ as

$$\gamma_p' \sim 5 \times 10^7\, \Gamma^{-1}\, E_{\nu,\mathrm{PeV}}^{\mathrm{ob}}. \qquad (1)$$

If the low-energy peak is attributed to proton-synchrotron emission, the peak frequency of the synchrotron emission, $\nu_{\mathrm{pk},1}$, obeys

$$h\nu_{\mathrm{pk},1}' = m_e c^2 \frac{m_e}{m_p}\left(\frac{B'}{B_{\mathrm{crit}}}\right)\gamma_p'^2, \qquad (2)$$

where $B_{\mathrm{crit}} \equiv 4.41 \times 10^{13}$ G is the critical magnetic field. Combining Equations (1) and (2) provides a constraint on the magnetic field,

$$B'|_{\mathrm{pk},1} = (7 \times 10^{-4}\ \mathrm{G})\left(\frac{\nu_{\mathrm{pk},1}^{\mathrm{ob}}}{10^{14}\ \mathrm{Hz}}\right)\left(\frac{\Gamma_{\mathrm{bulk}}}{10}\right)\left(\frac{E_\nu^{\mathrm{ob}}}{\mathrm{PeV}}\right)^{-2}. \qquad (3)$$

The peak frequency of the second hump in the SED relates to the peak energy of the secondary $e^\pm$ that results from either $\pi^\pm \to e^\pm$ decay or from $\pi^0 \to \gamma\gamma \to e^\pm$ reactions. It will be shown later that for PKS B1424-418, up to one generation of $e^\pm$ cascade is expected, so that for both channels, the energy of $e^\pm$ is $E_e \sim 0.05 E_p$. Reproducing the second hump with the observed peak frequency $\nu_{\mathrm{pk},2}^{\mathrm{ob}}$ from synchrotron emission of the secondary pairs requires a magnetic-field strength

$$B'|_{\mathrm{pk},2} = (3 \times 10^{-2}\ \mathrm{G})\left(\frac{\nu_{\mathrm{pk},2}^{\mathrm{ob}}}{10^{23}\ \mathrm{Hz}}\right)\left(\frac{\Gamma_{\mathrm{bulk}}}{10}\right)\left(\frac{E_\nu^{\mathrm{ob}}}{\mathrm{PeV}}\right)^{-2}. \qquad (4)$$

The value $B|_{\mathrm{pk},2}$ is clearly incompatible with $B|_{\mathrm{pk},1}$, which means that the proton model is not viable.

LH-psyn model: If we require a proton-synchrotron origin of the high-energy hump in the SED and a neutrino emission peaked at PeV energies, the requirement on the magnetic-field strength can be derived in a similar way as Equation (3):

$$B'_{\mathrm{psyn}} = (7 \times 10^5\ \mathrm{G})\left(\frac{\nu_{\mathrm{pk},2}^{\mathrm{ob}}}{10^{23}\ \mathrm{Hz}}\right)\left(\frac{\Gamma_{\mathrm{bulk}}}{10}\right)\left(\frac{E_\nu^{\mathrm{ob}}}{\mathrm{PeV}}\right). \qquad (5)$$

The magnetic energy density is then of the order of 10^8 erg cm^{-3}. Compared to the photon energy density for this source, $u_{\mathrm{phot}} \sim 6 \times 10^{-6} L_{46}^{\mathrm{iso}} R_{18}^{-2} \Gamma_1^{-4}$ erg cm^{-3}, it is clearly unphysical for the jet energy budget.

LH-π model: This scenario is slightly more complicated, but a few generic conditions must be met:

1. The proton-synchrotron flux must not exceed that of synchrotron radiation of primary electrons.
2. The Y_{SSC} parameter, defined as the power ratio of synchrotron-self Compton emission to synchrotron emission, must not exceed unity for this source (otherwise, the model becomes the SSC model).
3. The observed peak frequency of the high-energy hump in the SED $\nu_{pk,2}^{ob} \sim 10^{23}$ Hz must be consistent with the characteristic energy of the secondary $e^\pm$ from pγ interactions $E_e \sim 0.05\, E_p$, with E_p determined from the neutrino energy $E_{\nu,PeV}^{ob}$.
4. The emission from pairs through the BH process must not overshoot the observation.

Here, the SED is approximated by four segments of power-law spectra. The equations to calculate these four constraints are 1: Equation (26), 2: Equation (27), 3: Equation (18), and 4: Equation (22) from Appendix A. All four constraints are displayed in Figure 1 for a blob radius $R_{blob}' = 10^{18}$ cm. When R_{blob}' increases, the boundaries of the gray and green regions (corresponding to constraints 1 and 2, respectively) move toward the lower-left corner of the panel, whereas the regions defined by constraints 3 and 4 are independent of R_{blob}'. There is no region of overlap for all four constraints, whatever the value of R_{blob}', which rules out the LH-π model for PKS B1424-418.

SSC and LH-SSC models: In the Thomson scattering regime, the frequency of the scattered photon is $\nu_{pk,2}' \simeq \gamma_e'^2 \nu_{pk,1}'$. Scattering proceeds in the Klein–Nishina regime for electron Lorentz factors $\gamma' \gtrsim \gamma_{KN}'$, here $\gamma_{KN}' h\nu_{pk,1}' \sim m_e c^2$. Combining the two expressions, we find the following relationship among the Lorentz factors of the accelerated electrons in the comoving frame γ_e' and the SED parameters of PKS B1424-418:

$$\gamma_e' = 0.007\, \gamma_{KN}' \left(\frac{\nu_{pk,1}^{ob}}{10^{14}\text{ Hz}}\right)\left(\frac{\nu_{pk,2}^{ob}}{10^{23}\text{ Hz}}\right)\left(\frac{\Gamma}{10}\right)^{-1} < \gamma_{KN}'. \quad (6)$$

We conclude that the IC scattering of primary electrons is always Thomson scattering.

The comoving photon density can be written as

$$u_{ph}' = \left(\frac{d}{R_{blob}}\right)^2 \left(\frac{1+z}{\Gamma^2}\right)^2 \frac{\nu F_\nu}{c}. \quad (7)$$

Here, $d = 4.477$ Gpc is the comoving radial distance of the source (for $z = 1.522$ and a flat ΛCDM universe with $\Lambda = 0.7$), and $u_b' = B'^2/8\pi$ is the comoving magnetic-field energy density. We can express the constraints on B', R_{blob}', and Γ in terms of observed quantities as

$$R_{blob}'\Gamma \approx (1.4 \times 10^{19}\text{ cm})\, Y_{SSC}^{-1/2} \left(\frac{\nu F_\nu|_{pk,1}^{ob}}{10^{-11}\text{ erg cm}^{-2}\text{ s}^{-1}}\right)^{1/2}$$
$$\times \left(\frac{\nu_{pk,1}^{ob}}{10^{14}\text{ Hz}}\right)^{-2}\left(\frac{\nu_{pk,2}^{ob}}{10^{23}\text{ Hz}}\right) \quad (8)$$

and

$$B' \approx (9.2 \times 10^{-3}\text{ G})\left(\frac{\nu_{pk,1}^{ob}}{10^{14}\text{ Hz}}\right)^2\left(\frac{\nu_{pk,2}^{ob}}{10^{23}\text{ Hz}}\right)^{-1}\left(\frac{\Gamma}{10}\right)^{-1}, \quad (9)$$

where

$$Y_{SSC} \approx \frac{\nu' u_\nu'(\nu_{pk,1}')}{u_b'} \approx \frac{\nu F_\nu|_{pk,2}}{\nu F_\nu|_{pk,1}} \approx 10 \quad (10)$$

and u_ν' is the differential energy density of photons in the comoving frame. The scaling values of the observed quantities are typical for the SED of PKS B1424-418 (c.f., Figure 4). Therefore, Equation (8) implies that the blob radius is large, on the order of a light-year. The magnetic-field strength must be rather low, suggesting that the blob is located far away from the central engine, beyond the broad-line region and the dusty torus (see also Tavecchio et al. 2013). This scenario justifies the fact that we ignore the IC scattering of external photons.

The optical depth of MeV-band γ-rays to pair production, $\tau_{\gamma\gamma}$, can be estimated as

$$\tau_{\gamma\gamma} \approx \frac{L'}{R_{blob}'}\frac{\sigma_T}{4\pi m_e c^3} \approx 3 \times 10^{-5}\left(\frac{\nu F_\nu^{ob}}{10^{-11}\text{ erg cm}^{-2}\text{ s}^{-1}}\right)$$
$$\times \left(\frac{\Gamma}{10}\right)^{-4}\left(\frac{R_{blob}'}{10^{18}\text{ cm}}\right)^{-1}, \quad (11)$$

indicating that MeV γ-rays can escape the source. A numerical calculation on the optical depth shows that $\tau_{\gamma\gamma}$ approaches unity for multi-TeV to PeV γ-rays for typical model parameters for PKS B1424-418, which is consistent with one cascade generation of these γ-rays.

The position and flux of the high-energy peak in the SED need to be explained by the SSC model. Determining the permitted abundance of hadrons as well as the detailed fitting of the entire SED and the neutrino data require the numerical modeling of the source, which is discussed in the following section.

PKS B1424-418 exhibits significant time variabilities over a wide range of scales, as other FSRQs and BL Lacs do. Variability timescales t_{var}^{ob} as short as a month are consistent with the causality argument $t_{var}^{ob} \sim R_{blob}'(1+z)/\Gamma c$ and the constraint set by Equation (8) for a blob size $R_{blob} = 7.5 \times 10^{17}$ cm and a bulk Lorentz factor $\Gamma = 35$, for which $t_{var}^{ob} \simeq 3$ weeks.[4] Faster variability has been observed on timescales shorter than a day, which may be explained by compact substructures in the jet, such as recollimation (Bromberg & Levinson 2009), "jet in a jet" scenarios, or magnetic reconnection (Giannios et al. 2009; Giannios 2013). In any case, explaining this very fast variability is beyond the scope of this paper.

## 3. Numerical SED Model and the Consequences for Neutrino Production

We present our numerical simulation results for the SSC and LH-SSC scenarios here, which were found to be preferable in the previous section. After discussing our methods, we will first discuss the Burst phase, and then show a self-consistent picture for the evolution of the blazar over the full timeline studied.

---

[4] This choice of Γ is also in line with the best-fit spectra from numerical simulations over the parameter space.

Table 2
List of Parameters and Notations

	Group	Symbol	Definition
Parameters	Global	$R'_{\rm blob}$	Comoving radius of blob, fixed to 7.5×10^{17} cm
		$f_{\rm esc}$	$e^\pm$ and p escape fraction, fixed to $1/10$
		$\Gamma_{\rm bulk}$	Bulk Lorentz factor of the blob fixed to 35
	Leptonic	B'	Magnetic field strength, blob frame
		$L_{e,\rm inj}$	Injection luminosity of primary e^-, AGN frame
		$\gamma'_{e,\rm min}$	Minimum Lorentz factor of primary e^-, blob frame
		$\gamma'_{e,\rm max}$	Maximum Lorentz factor of primary e^-, blob frame
		$\alpha'_{e,\rm idx}$	Power-law index of injected primary e^-
	Hadronic	$\alpha'_{p,\rm idx}$	Power-law index of injected protons, fixed to -2.0
		η_b	Luminosity ratio p to e^- at injection, i.e., $\eta_b \equiv L_{p,\rm inj}/L_{e,\rm inj}$
		$E^{\rm ob}_{p,\rm max}$	Maximum energy of injected protons, observer frame
Notations		$P_{0,1,0}(E_{p,\rm max}, \eta_b)$	Probability to observe 0, 1, and 0 neutrino events in the 0.5–1.6 PeV, 1.6–2.4 PeV, and >2.4 PeV bands in IceCube, respectively, as a function of $E_{p,\rm max}$ and η_b
		$P_{\nu,\rm max}$	Maximum value of $P_{0,1,0}(E_{p,\rm max}, \eta_b)$ in the parameter space, named "neutrino best fit"
		L_ν	Total neutrino luminosity, including all flavors
		L_γ	γ-ray luminosity integrated over the frequency band $10^{18.1} \sim 10^{24.4}$ Hz
		+	SED best-fit mark
		×	Neutrino best-fit mark, global
		⊗	Neutrino best fit under the constraint of the SED being reproduced within 3σ confidence
		✳	Joint best-fit mark, for SED and neutrino
		☉	Neutrino flux to expect one >0.5 PeV event during the 2LAC phase, assuming the same effective area of IceCube as in the IC-2yr and Burst phases (see Figure 5)
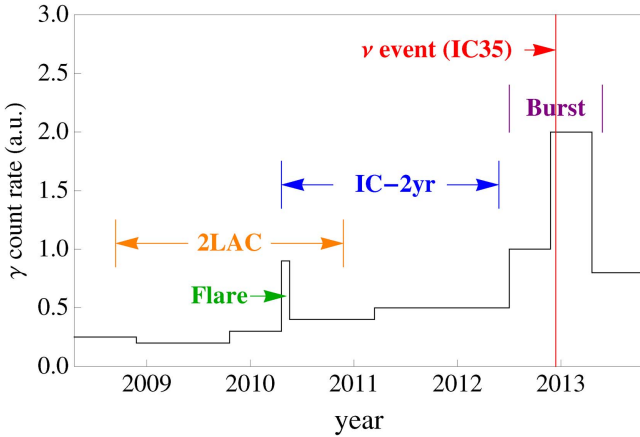
Figure 2. Illustration of the γ-ray count rate as a function of time together with a definition of the 2LAC, IC-2yr, and Burst phases of PKS B1424-418. Note that the count rate is meant for illustrative purposes only and does not accurately reflect the data (see Figure 1 of K16 for the bi-weekly binned γ-ray light curve). Also note that K16 shows the SED from the three-year IceCube phase, which overlaps with the Burst phase. The IC-2yr SED, constructed and provided by the authors of K16, is not shown in their paper.

3.1. Numerical Methods

We simulate time-dependent particle spectra for $e^\pm$, p, n, γ, and ν_α (α denotes the neutrino flavor) by numerically solving the time-dependent differential-integral kinematic-equation system in the energy space γ, for all the particle species mentioned above:

$$\partial_t n(\gamma, t) = -\partial_\gamma\{\dot{\gamma}(\gamma, t)n(\gamma, t) - \partial_\gamma[D(\gamma, t)n(\gamma, t)]/2\} - \alpha(\gamma, t)n(\gamma, t) + Q(\gamma, t),$$

$$(12)$$

where $n(\gamma) \equiv d^2N/d\gamma dV$ is the differential number density of the particle species. In the equation above, the source term Q may depend on energy γ, time t, and the current target-particle distributions $\{n_{\rm tar}(\gamma)\}$. It models the injection, emission, or generation of a new particle after an interaction, or a redistribution or re-injection of the same particle after scattering. The sink term α depends on the same set of variables and functionals, which models the escape, decay, annihilation, and disappearance of the particle from the blob due to an interaction. The differential terms $\dot{\gamma}(\gamma, t)$ and $D(\gamma, t)$ account for the particle cooling and diffusion effect in momentum space due to synchrotron radiation, Thomson scattering, and the BH process. In those processes, the electron or proton loses a tiny fraction of energy after scattering, and the finiteness of the numerical grid spacing is unable resolve this tiny shift in the redistribution function via the terms α and Q. Therefore, we apply the "continuous-loss" approximation, demanding an accuracy up to second-order differentiation. Due to isotropy and spherical symmetry, only the radial component $D(\gamma, t)$ of the diffusion tensor appears in the equation.[5]

The rates and redistribution functions are described by physics, where we consider the synchrotron, IC, pair production and annihilation, photohadronic ($p\gamma$) interaction, and BH (photo-pair) processes. See Appendix B for details and Hümmer et al. (2010, hereafter H10) for the simplified $p\gamma$ interaction model, which we apply in this paper.

Bremsstrahlung and pp collisions are ignored in our case, which can be relevant in blazars when the emission region

---

[5] The mathematical forms of this treatment are expressed in Equations (40)–(42), Equations (69)–(71), and Equation (87).
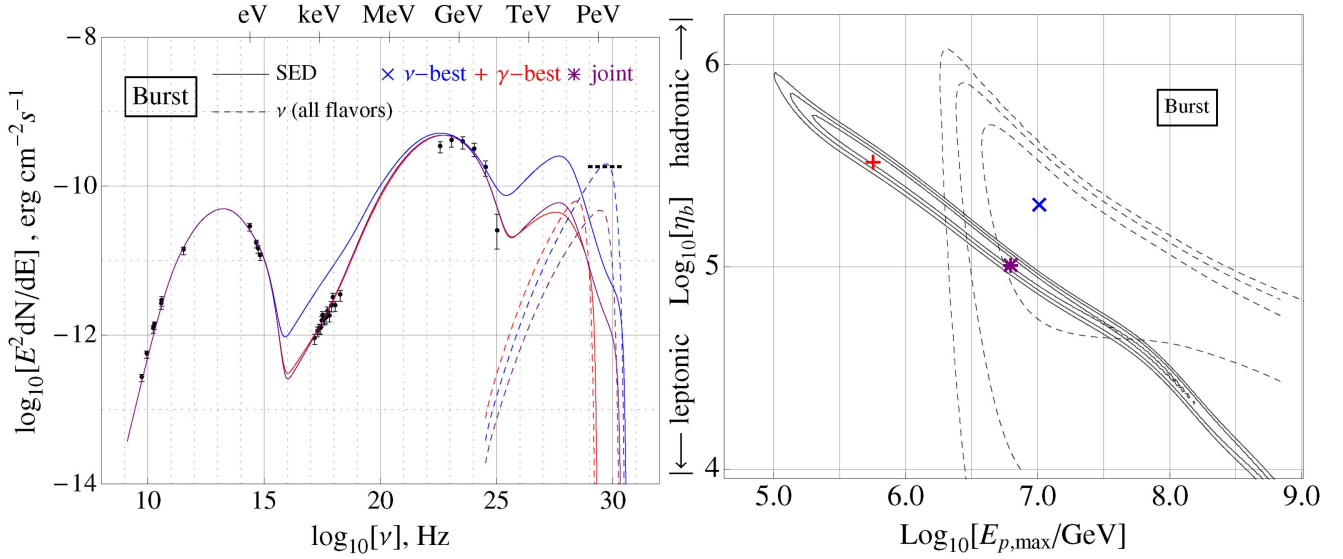
Figure 3. Right panel: fitting quality to SED and neutrino observations over the $E_{p,\max}$ and $\eta_b = L_{p,\mathrm{inj}}/L_{e,\mathrm{inj}}$ parameter space for the Burst phase. Solid contours are the boundaries of 1σ, 2σ, and 3σ confidence regions for the SED fit, while dashed curves are the iso-probability contours for $P/P_{\nu,\max} = 0.32$, 0.05, 0.003—see the main text for details. The symbols $+$, $\times$, and $*$ mark the best-fit parameters of the SED, neutrino, and the joint fits, respectively. Left panel: the SED (solid) and neutrino (dashed) spectra, corresponding to the three marks on the right panel. The horizontal dashed line is the neutrino flux level to observe one PeV event over this nine-month period. Data points are provided from the authors of K16.

is compact (Eichmann et al. 2012). However, in our case, the large blob size leads to a low number density of cold protons, which can be easily estimated as $n_{p,\mathrm{cold}} \sim 2.5 \times 10^{-5}\eta_{p,\mathrm{cold}}R_{18}^{-2}\Gamma_{1.5}^{-4}L_{46}^{\mathrm{ob}}$. Here, L^{ob} is the photon luminosity in the observer frame, and we have parameterized the energy density of cold protons as a multiple $\eta_{p,\mathrm{cold}}$ of photons. Adopting the zeroth-order approximation on the pp cross-section, $\sigma_{\mathrm{pp}} \sim 50$ mb, the optical depth of pp collision is estimated o be $\tau_{\mathrm{pp}} \sim 10^{-12}\eta_{p,\mathrm{cold}} R_{18}^{-1}\Gamma_{1.5}^{-4}L_{46}^{\mathrm{ob}}$, which is negligible. The energy-loss rate due to bremsstrahlung is estimated by Eichmann et al. (2012) to be $\dot{\gamma}_{\mathrm{brem}}/\gamma \sim 1.4 \times 10^{-16}(\ln 2 - 1/3)n_{p,\mathrm{cold}} \sim 1.3 \times 10^{-21}\eta_{p,\mathrm{cold}}R_{18}^{-2}\Gamma_{1.5}^{-4}L_{46}^{\mathrm{ob}}$, which is significantly below that of the synchrotron loss rate $\dot{\gamma}_{\mathrm{syn}}/\gamma \sim 10^{-12} B_{-3}^{2}\gamma_3$ even for the lowest-energy electrons in our case.

We use the finite-difference method to solve the equation numerically, on an evenly spaced logarithmic grid in energy and a linear one in time. The "Crank–Nicolson" differential scheme is used in time with the "Chang & Cooper" (Chang & Cooper 1970) scheme in energy to achieve stability and a more accurate goal in the correct steady-state solution. For the compatibility with the latter scheme as well as increased accuracy, we calculate up to the second-order differential term from the physics. See Appendix C for details and Vurm & Poutanen (2009, hereafter VP09) for the application to leptonic processes. Our list of input parameters and assumptions is summarized in Table 2, which we describe in greater detail in this and the next sections.

The dynamical SEDs of PKS B1424-418 reported in K16 are categorized into four phases: (1) a flare in 2010, lasting about one month, (2) 2LAC phase, from 2008.8 to 2010.9, (3) IC-2yr period, from 2010.5 to 2012.5, the first two years of IceCube observations; (4) Burst phase, from 2012.6 to 2013.3, when the source experienced a long-lasting high-flux phase in γ-rays. Figure 2 provides a visual timeline, including the time-averaged GeV-band γ-ray flux. A 2 PeV neutrino event in IceCube (IC35, also dubbed "Big Bird") was observed on 2012 December 4, during phase 4, with a position consistent with

that of PKS B1424-418. The SEDs shown in K16 are based on time-averaged spectra from each phase. In this paper, the flare phase is ignored since its duration was too short to result in a neutrino fluence comparable with that of other phases.[6] We therefore focus on three phases (2LAC, IC-2yr, and Burst), as indicated in Figure 2, which can be interpreted as the time-dependent evolution of the AGN. We will first simulate the phases independently, and then interpret the evolution (changes) of the parameters.

For each phase, the SED and neutrino spectra are modeled by a steady-state solution to Equation (12). Under the SSC and LH-SSC scenarios, the first peak of the SED is described as synchrotron emission from primary e^-, and the γ-rays are described as SSC emission from the same e^- population (see Table 1). After fixing a few global parameters such as R_{blob} and Γ_{bulk}, the following two-step simulations are performed for each of the three phases of PKS B1424-418 (2LAC, IC-2yr, and Burst). (1) Use leptonic simulations ($\eta_b \equiv 0$) to find the best-fit parameters of the primary e^- for the low-energy hump and γ-ray band (10^{22}–10^{25} Hz). (2) Inject protons until their spectrum reaches a steady state to find the total SED and neutrino spectrum.

In step 1, with leptonic simulations, the following parameter space is scanned: $L_{e,\mathrm{inj}}(10^{42.5} \sim 10^{45.5}$ erg s$^{-1}) \otimes \gamma'_{e,\min}$ $(10^{2.6} \sim 10^{3.9})$ $\otimes \gamma'_{e,\max} (10^{4.2} \sim 10^{6.0}) \otimes \alpha_{e,\mathrm{inj}}(-2.0 \sim -1.0) \otimes B'(10^{-2.2} \sim 10^{-4.0}$ G) $\otimes \Gamma_{\mathrm{bulk}}(1 \sim 200)$. The best-fit parameters are obtained by χ^2-minimization.

In step 2, including protons, the SED and the neutrino spectrum are calculated for a logarithmic $\eta_b(10^2 \sim 10^8) \otimes E'_{p,\max} (10^2 \sim 10^9$ GeV) parameter grid for each phase of PKS B1424-418. Here, η_b is the proton-to-electron luminosity ratio (baryonic loading) at injection, $\eta_b = L_{p,\mathrm{inj}}/L_{e,\mathrm{inj}}$, and

---

[6] Even for the most optimistic estimates in K16, the expected neutrino count is far below 1.0, consistent with the null detection of neutrinos during this phase.

$E'_{p,\max}$ is the maximum proton energy. Each point of the grid corresponds to a unique combination of η_b and $E_{p,\max}$, and therefore an independent simulation. The entire grid has a resolution of 400×160 for each phase, requiring a total of 192,000 hadronic simulations.

The global parameters $R'_{\rm blob} = 7.5 \times 10^{17}$ cm and $\Gamma_{\rm bulk} = 35$ are chosen according to Equation (8), including a variability time $t_{\rm var} < 1$ month. The energy-independent escape rate for e^- and p is assumed to be $t_{e,p}^{-1} = 0.1\, t_{\rm fs}^{-1}$, which is an order of magnitude slower than the free-streaming escape rate (that of the neutrinos). We also use a fixed power-law injection index $\alpha_{p,\rm inj} = -2.0$ for proton injection, where the results are not very sensitive to this value.

TANAMI VLBI data of PKS B1424-418 indicate an angular size of a few milli-arcsecond for the emission region in the radio band, which translates into a physical size of about the order of a few 10^{19} cm, which is larger than that of the blob. The extended VLBI component can be interpreted as synchrotron emission from electrons that escaped from the blob into an extended region of size $R_{\rm ext} \sim 3.0 \times 10^{19}$ cm that is filled with a weaker magnetic field $B'_{\rm ext} \simeq 0.1\, B'_{\rm blob}$. We assume that the radio data are fitted by synchrotron emission from electrons that escaped the blob into an extended region using these parameters. All other contributions to the SED come from the blob.

3.2. SED Model and Neutrino Production, the Burst Phase

In this subsection, we focus on the Burst phase and the relationship to the potentially observed neutrino event during that phase.

For each parameter-space simulation, we perform independent optimizations. First, we adapt our model to the SED and find the best fit and confidence regions by calculating the reduced χ^2 values.[7] This SED best fit is marked with the symbol "+." Then, with the predicted neutrino spectrum from each simulation, we calculate the probability, $P_{010}(E_{p,\max}, \eta_b)$ of observing 0, 1, and 0 neutrino events from PKS B1424-418 with IceCube, as indeed observed in the (0.5–1.6), (1.6–2.4), and >2.4 PeV energy bands, respectively. In each band, the expected number of neutrino events follows a Poisson distribution. The best adaptation to the neutrino data without regard for the SED is marked by the symbol "×," and its fit probability is denoted by $P_{\nu,\max}$. The joint best-fit point, by maximizing the joint probability of the SED and neutrino fits, is marked with the symbol "✳."

We find that both SED and neutrino fits independently prefer large baryonic loadings for the Burst phase, which may point toward a baryonically loaded burst. At the neutrino and joint best-fit points in Figure 3 (×, ✳), the associated proton maximum energies are around 10 PeV, which is consistent with the observed PeV neutrino event. However, the maximum proton flux at the neutrino best fit, ×, is in tension with the X-ray data, which we will demonstrate below.

We show the SED for the SED best fit (+), the joint best fit (✳), and the neutrino best fit (×) in the left panel of Figure 3. We clearly observe that the SED is in tension with the data in
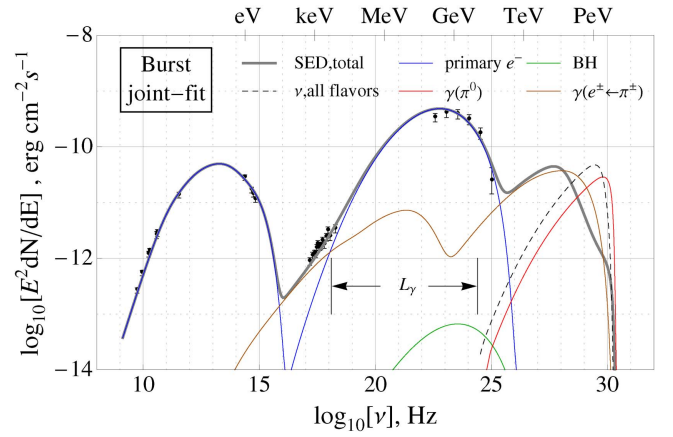

Figure 4. Components for the joint best-fit SED during the Burst phase. Gray: total SED; blue: emission from primary e^-; green: emission from pairs generated via the BH process; brown: γ-ray injection spectrum from $e^\pm$ pairs via $\pi^\pm$ decay; Red: γ-ray injection spectrum from π^0 decay; black dashed curve: neutrino, all flavors. The fractional contributions of these components to the L_γ band are $L_{\rm ssc} = 0.981$, $L_\pi = 0.0185$, $L_{\rm BH} = 1.3 \times 10^{-4}$, respectively, where L_γ is defined as the integrated luminosity between $10^{18.1} \sim 10^{24.4}$ Hz (5 keV–10 GeV). The bolometric neutrino to gamma-ray luminosity ratio is $L_\nu/L_\gamma = 0.051$. The $\gamma\gamma$-absorption effect in the source becomes significant above $\sim$100 TeV, which is manifested in the suppression of the total SED in that energy band. The data points here and in Figures 3, 5, and 6 are provided by K16 (processed from data from *Fermi*-LAT, Swift-XRT/UVOT, SMARTS, and the LBA, etc.; see the supplementary material for the data analysis methods in K16).

the X-ray energy range. On the other hand, the SED is described reasonably well for the other two fit points. Note that the radio data are fitted from the extended emission region.

As a next step, we address the question whether the observed neutrino event can come from the Burst phase of PKS B1424-418, as reported in K16. One test of this hypothesis is energetics—in K16, the neutrino luminosity was directly related to the section of the SED we defined "L_γ" in the caption of Figure 4, One can easily see that this energy range is dominated by leptonic processes (1) in our model, contrary to what has been assumed in K16 (for which hadronic processes 2–4 would need to dominate that energy range).

We list the fractional contributions of the different physical interactions to the SED for the joint best-fit case of the Burst phase in the caption of Figure 4, where one can clearly read off that the SSC contribution dominates. We also show the neutrino-to-γ-ray ratio L_ν/L_γ, which is of order 5% for the models fitting the SED. These numbers are to be interpreted as an additional "theory" correction factor in addition to those included in K16 (independent of the spectral correction in K16, which would reduce this number). They reflect the fact that hadronic processes only dominate in a small portion of the energy range marked "L_γ" in Figure 4, considering that the second hump cannot be dominated by hadronic processes. Note that hadronic components contribute significantly to the SED outside the pre-defined energy range of L_γ ($10^{18.1} \sim 10^{24.4}$ Hz, 5 keV to 10 GeV). In K16, the predicted number of neutrino events in the 1.0–2.0 PeV bin is 1.6, assuming that the entire second hump is generated from hadronic processes. From our model, this needs to be corrected by this factor of 0.05, arriving at $\sim$0.08 events. Consistently, the neutrino spectrum from our numerical simulation (the joint best-fit case) predicts 0.094 events in IceCube within the same energy bin.

---

[7] The data points and statistical error bars are provided by K16. For total errors, we supplement an estimated systematic error of around 10% for the radio to X-ray bands so that the data can be well described by power laws. For *Fermi*-LAT, the systematic error is dominated by the uncertainties of the effective area for Pass7 data, which is roughly 10% to 15%, depending on energy.
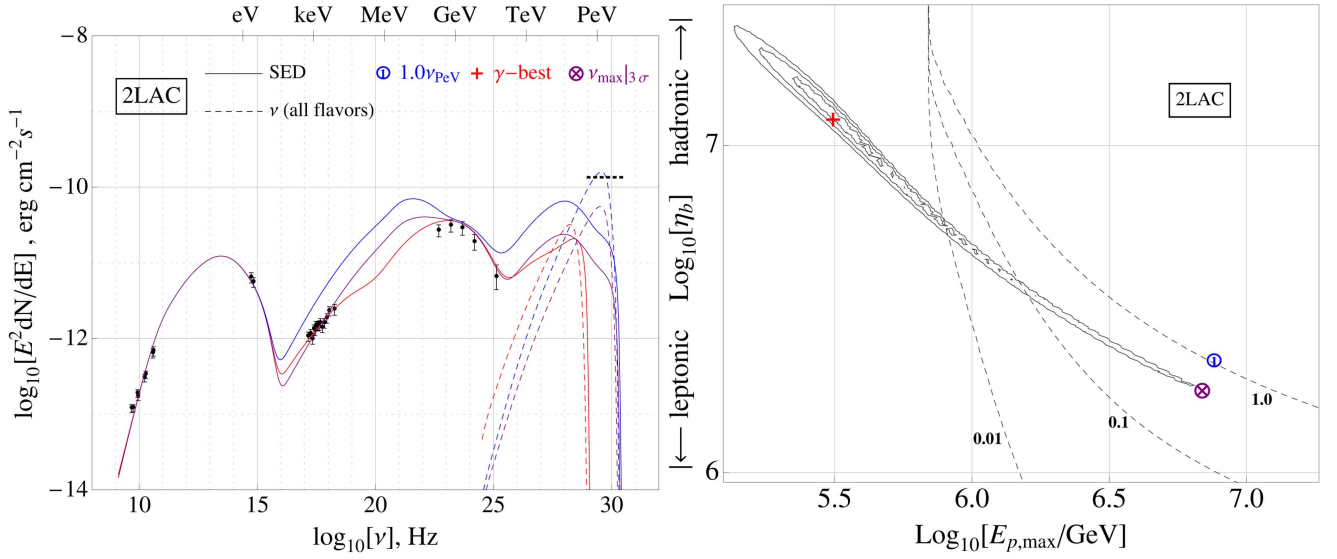
Figure 5. Right panel: fitting to the SED with $1–3\sigma$ confidence regions (boundaries in solid curves) and iso-neutrino event (between 0.5 and 2.4 PeV) contours (dashed). ① is the mark for the maximum neutrino production within the 3σ region and ✳ is a representative point on the one-neutrino event contour. Left panel: the corresponding SED (solid) and neutrino (dashed) spectra for those three marks on the right panel. The short horizontal dashed line is the neutrino flux level to expect one PeV event in the IC40+59 configuration during this phase.

Table 3
Parameters and the Expected Number of Neutrino Events in IceCube for the Best-fit Models During Each Phase

| Phase	2LAC			IC-2yr			Burst		
Time	2008.9–2010.9			2010.5–2012.5			2012.6–2013.3		
$R_{\mathrm{blob}}/\mathrm{cm}$				7.5×10^{17}					
Γ_{bulk}				35					
B'/mG	2.5			2.0			2.5		
$L_{e,\mathrm{inj}}/L_{\mathrm{edd}}$	6.7×10^{-5}			1.2×10^{-4}			3.2×10^{-4}		
$\gamma'_{e,\mathrm{min}}$	1.8×10^{3}			1.8×10^{3}			2.2×10^{3}		
$\gamma'_{e,\mathrm{max}}$	1.3×10^{5}			8.9×10^{4}			1.0×10^{5}		
$\alpha'_{e,\mathrm{idx}}$	-2.2		-2.2				-1.8		
$\alpha'_{p,\mathrm{idx}}$				-2.0					
Fit symbol	$+$	$\otimes$	①	$+$	✳	$\times$	$+$	✳	$\times$
Fit	SED	Table 2	Table 2	SED	joint	ν	SED	joint	ν
$\eta_b/10^6$	11.5	1.8	2.2	2.3	0.76	0.72	0.33	0.10	0.20
$E_{p,\mathrm{max}}^{\mathrm{ob}}/\mathrm{PeV}$	0.37	7.5	8.3	0.68	6.8	11.2	0.68	7.5	12.3
N_ν, 0.5–1.6 PeV	0	0.35	0.74	0.0090	0.62	0.79	0.0045	0.21	0.76
N_ν, 1.6–2.4 PeV	0	0.082	0.18	0	0.13	0.22	0	0.042	0.22
N_ν, >2.4 PeV	0	0.037	0.10	0	0.044	0.21	0	0.018	0.24
$P_{0,1,0}$, %	…	…	…	0	5.7	6.5	0	3.2	6.4
Photon SED χ^2/d.o.f.	0.83	1.36	86.9	1.82	1.94	7.10	1.38	1.40	171

Note. $P_{0,1,0}$ next to the bottom row is the joint probability of observing 0, 1, and 0 neutrino events in the three energy bins above. See Table 2 for the definition of symbols and notations.

3.3. SED and Neutrino from the 2LAC and IC-2yr Phases, and Variation in Activity States

Let us now address if we can draw a self-consistent picture of the AGN blazar over time. For that purpose, we independently fit the parameters for the three phases 2LAC, IC-2yr, and Burst in Figure 2; these fits are shown in Figures 3, 5, and 6. For the IC-2yr phase, we predict neutrino events in the same format as the one in the Burst phase, even though no neutrinos are detected during this phase. The

purpose is to demonstrate that the correlation between the PeV neutrino event with the Burst phase is weak. Indeed, the IC-2yr phase predicts up to a probability $P_{0,1,0} = 5.7\%$ of producing the same observations in IceCube, compared to $P_{0,1,0} = 3.2\%$ in the Burst phase (see Table 3). The relative probability is therefore $P_{0,1,0}(\mathrm{IC\text{-}2yr})$: $P_{0,1,0}(\mathrm{Burst}) = 1.6{:}1$. Here $P_{0,1,0}$ is defined as the joint probability of observing 0, 1, and 0 neutrino events in the 0.5–1.6, 1.6–2.4, and >2.4 PeV energy bins, respectively, where in each bin, the
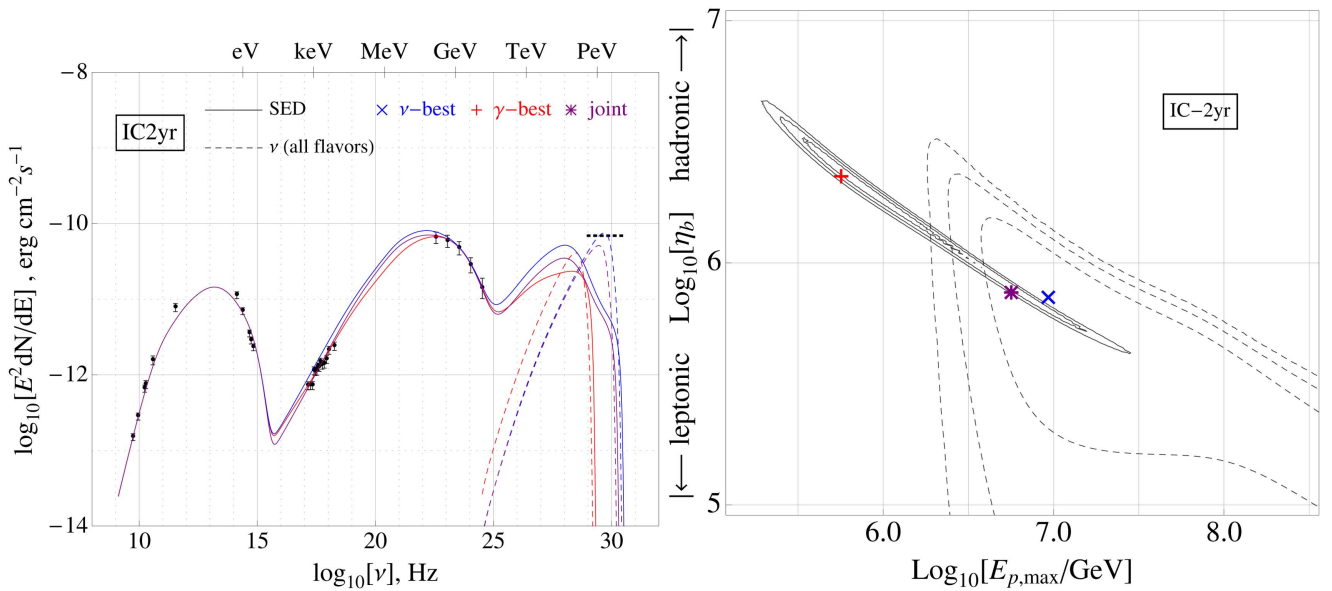
Figure 6. Fitting quality (right panel) and the corresponding SED + neutrino spectra (left panel) for the best-fit marks. The conventions for the curves and symbols are the same as those in Figure 3.

expected number of neutrino events follows a Poisson distribution.

For the 2LAC phase, IceCube was operating with mainly the IC40+59 configuration, compared to the full IC86 for the other phases. Here we show the contours of the predicted neutrino events of >0.5 PeV during this phase in the parameter space, from the IC40+59 configuration. The best-fit point for the SED in Figure 5 is marked with "+," the maximum neutrino flux within the 3σ region for the SED fit is marked by "⊗," and a representative point on the $N_\nu = 1$ contour is picked and marked with "①." Since the SED of the 2LAC phase has a lower photon flux than that of the IC-2yr or Burst phase, a lower target photon density in the source is implied. In order to have a sufficiently large $p\gamma$ interaction rate to produce the right amount of X-rays and one neutrino event, the required proton-to-lepton luminosity ratio η_b has to be very large: $\eta_b \gtrsim 10^6$. From that perspective, it is not surprising that no neutrinos were observed during that phase.

The X-ray band, seen as the gap between the two humps in the SED, is a mixture of leptonic and hadronic components, as shown in Figure 4. Hadronic secondary emission depends on the detailed processing of the electromagnetic cascades in the source, mainly via the following channels: $p\gamma \rightarrow \pi^0 \rightarrow \gamma\gamma \rightarrow e^\pm$, $p\gamma \rightarrow \pi^\pm \rightarrow \mu^\pm \rightarrow e^\pm$, and $p\gamma \rightarrow p + e^\pm$. In the π^0 channel, the emission predominantly comes from the first generation of pairs. The source itself becomes optically thick for γ-rays above roughly 100 TeV. It was further estimated by Stecker et al. (2012) that the spectrum above $\sim$100 GeV will suffer from additional suppression due to absorption by EBL, but this effect does not play a significant role in our fitting.

We list the detailed best-fit parameters and expected number of neutrino events during each phase in Table 3. We note that the parameters for the magnetic fields, and the minimum and maximum energies for the e^- and p injections, are very similar. The SEDs evolving from the earliest phase, 2LAC, to IC-2yr, and finally to the Burst phase can be simply reproduced by an increase of the e^- versus p injection rate with time, and a slight hardening effect on the e^- injection spectrum.

The proton-to-lepton luminosity ratio required to fit the neutrino result is large, of the order of 10^5–10^6. This value is coincidentally similar to that found for other blazars, such as by Diltz et al. (2015) and Petropoulou et al. (2015). In our case, on one hand, the $p\gamma$ interaction rate is lower than those in the above cases and more protons are needed to achieve the same level of γ-rays; on the other hand, compared to their LH-π models, we only need a subdominant hadronic contribution to γ-rays, which lowers the requirement for proton luminosity. The physical proton-injection luminosities needed for these values are around a few times the Eddington luminosity. This requirement can be alleviated if we assume a lower escape rate for protons, e.g., a magnetic configuration that can trap the protons longer in the blob. In our model, due to the low $p\gamma$ efficiency, most protons simply escape without having a $p\gamma$ interaction and the interactions cause no visible effects on the proton spectrum. Therefore, the required $L_{p,\text{inj}}$ scales linearly with the escape rate.

4. Summary and Conclusions

A potential correlation between the PeV neutrino event "Big Bird" by IceCube in 2012 and the Burst phase of the FSRQ PKS B1424-418 was reported by K16. That analysis relies on the frequently used assumption $L_\gamma \approx L_\nu$. In this paper, we have revisited this important relationship with a self-consistent one-zone emission model, with SEDs measured from three phases of the source: 2LAC (2008.8–2010.9), IceCube 2 year (IC-2yr, 2010.5–2012.5), and Burst (2012.6–2013.3). These different SEDs can be interpreted from our results as the variations of the blazar properties over time. We have also studied the parameter values needed to attribute the Burst phase to the neutrino event, which was observed in the IC-2yr phase and within it.

We found that the "conventional" hadronic model (high-energy hump via hadronic processes; the "LH-π" or "LH-psyn" model) does not work for this blazar, which is different from many other blazars, such as the well-studied Mrk 421 (Dimitrakoudis et al. 2014; Petropoulou et al. 2016), for which the high-energy hump of the SED can be fully accounted for by

hadronic processes. Therefore, the leading contribution to the SED of PKS B1424-418 must be leptonic. We have, however, shown that a subdominant hadronic contribution can be present. In terms of neutrino production, it is therefore an interesting question how much baryonic loading can be tolerated, even in an SSC model, without affecting the shape of the SED.

We have found that the observed one-neutrino event reported by K16 during the Burst phase is in tension with the SED fits, whereas up to ∼0.3 above-PeV events are acceptable. The probability of producing 0, 1, and 0 neutrinos in the 0.5–1.6, 1.6–2.4, and >2.4 PeV bins, respectively, as observed by IceCube, is up to 5.7% in the IC-2yr phase and 3.2% in the Burst phase. This suggests a chance coincidence of the observed PeV event with the Burst phase of PKS B1424-418, since there is an even higher probability of it occurring during the two-year IceCube observation than during the Burst phase. Our predicted event rates are consistent with K16 if their expectation is corrected for a small fraction of photon energy flux in the second peak that comes from hadronic processes. This means that an additional "theory correction factor" has to be applied if the gamma-ray and neutrino fluxes are to be correlated, which can only come from self-consistent models.

We have also demonstrated from independent simulations of the different phases of the blazar that a self-consistent time-dependent evolution picture can be drawn, meaning that the different phases can be described by similar parameters. We noted that the active state (Burst phase) can be achieved simply by increasing the injection rate of electrons and protons. It is the data in the X-ray range which sets constraints on the baryonic loading.

Although our results apply to PKS B1424-418 specifically, we emphasize the importance of a self-consistent description of the SED as opposed to generic approaches relating the gamma-ray and neutrino luminosities. The studied blazar serves as a counterexample for the direct correlation of these luminosities, which means that this assumption does not hold in general and has to be used with care. We have also quantitatively presented an example on how the neutrino observation, even with one candidate event, is able to break the degeneracies of blazar models.

Appendix A
Analytical Constraints

For brevity, all quantities are expressed in the blob comoving frame, unless annotated by a superscript "ob." The characteristic energy of the proton is constrained by the observed PeV neutrino event as

$$\gamma_{p,\text{char}} \sim E_\nu m_p c^2 / K_\nu , \qquad (13)$$

where $E_\nu = E_\nu^{\text{ob}}(1 + z)/\Gamma$ is the energy of the neutrino and $K_\nu \sim 0.05$ is the characteristic ratio of $E_p : E_\nu$ from the $p\gamma$ interaction. The $p\gamma$ event rate, per physical volume, estimated via the $\Delta^+(1232)$ resonance, is

$$\dot{N}_{p\gamma} \sim c\sigma_{p\gamma} f_{\text{ph}}(\varepsilon_{p\gamma,t}) f_p(\gamma_{p,\text{char}}), \qquad (14)$$

where $\sigma_{p\gamma} = 5.0 \times 10^{-28}$ cm^2 is the cross-section, $f_i(E_i) \equiv E_i \frac{dN_i}{dE_i}$ is the number density of particle i around E_i (f_{ph} is the photon density derived from the observed SED), $\varepsilon_{p\gamma,t} \sim \varepsilon_{p\gamma,\text{th}} \gamma_{p,\text{char}}^{-1}$ is the target photon energy, and $\epsilon_{p\gamma,\text{th}} \sim 0.3$ GeV is the position of the Δ resonance in the energy axis.

The injection rate in terms of the energy density of all pions due to $p\gamma$ interaction is

$$\dot{u}_\pi = \dot{N}_{p\gamma} E_p K_{p\gamma} , \qquad (15)$$

where $K_{p\gamma} \sim 0.2$ is the average inelasticity for the proton in $p\gamma$ interaction, and $E_{p,\text{char}}$ and $\dot{N}_{p\gamma}$ are computed from Equation (13) and Equation (14), respectively.

The luminosity of the second hump is given by the synchrotron photons from the secondaries as a result of pion decay,

$$L_{\text{ph},2} \sim \alpha_{\text{fs}} \varepsilon_2 f_{\text{ph}}(\epsilon_2) V_{\text{blob}} \sim K_{\pi \to e} \dot{u}_\pi V_{\text{blob}}, \qquad (16)$$

where $K_{\pi \to e} \sim 1/8$ (or higher, up to 5/8, if all γ-rays from π^0 decays are absorbed in situ) is the fraction of energy transferred to $e^\pm$ from π decays and $\alpha_{\text{fs}} = 4c/(3R)$ is the escape rate of the photons in the free-streaming case. Combining Equation (15) and Equation (16), we obtain the constraint on the steady-state proton number density around the energy $E_{p,\text{char}}$,

$$f_p(\gamma_{p,\text{char}}) = \frac{\alpha_{\text{fs}}}{c\sigma_{p\gamma}} \frac{\varepsilon_2}{E_{p,\text{char}}} \frac{f_{\text{ph}}(\varepsilon_2)}{f_{\text{ph}}(\varepsilon_{p\gamma,t})} \frac{1}{K_{p\gamma} K_{\pi \to e}}, \qquad (17)$$

together with the synchrotron peak energy from the secondaries in units of $m_e c^2$,

$$\varepsilon_{p\gamma,\text{pk}} = F_b \gamma_{p\gamma,e}^2, \qquad (18)$$

where $\gamma_{p\gamma,e} = r_m^{-1} K_{p\gamma} K_{\pi\to e} \gamma_{p,\mathrm{char}}$.

The injection rate of the energy density of pairs via the BH effect is estimated as

$$\dot{u}_{e,\mathrm{bh}} = c\sigma_{\mathrm{bh}} K_{\mathrm{bh}} f_{\mathrm{ph}}(\varepsilon_{\mathrm{bh},t}) f_p(\gamma_p) E_{p,\mathrm{char}}, \tag{19}$$

where σ_{bh} is the cross-section of the BH process and K_{bh} is the inelasticity. Both are dependent on the energy of the incident photon in the proton rest frame; however, their product has a peak value of

$$\sigma_{\mathrm{bh}} K_{\mathrm{bh}} \sim 1.5 \ \mu\mathrm{b} \tag{20}$$

at the proton rest-frame photon energy,

$$\varepsilon_{\mathrm{bh},r} \sim \gamma_{p,\mathrm{char}} \varepsilon_{\mathrm{bh},t} \sim 25 m_e c^2. \tag{21}$$

Substituting Equation (17) into the equation above, we obtain the luminosity of the synchrotron photons from those pairs as

$$\varepsilon_{\mathrm{bh,pk}} f_{\mathrm{bh}}(\varepsilon_{\mathrm{bh,pk}}) = \frac{\sigma_{\mathrm{bh}}}{\sigma_{p\gamma}} \frac{K_{\mathrm{bh}}}{K_{p\gamma} K_{\pi\to e}} \frac{f_{\mathrm{ph}}(\varepsilon_{\mathrm{bh},t})}{f_{\mathrm{ph}}(\varepsilon_{p\gamma,t})} \varepsilon_2 f_{\mathrm{ph}}(\varepsilon_2), \tag{22}$$

where the peak energy of the synchrotron photons from those pairs is

$$\varepsilon_{\mathrm{bh,pk}} = F_b \gamma_{e,\mathrm{bh}}^2 \tag{23}$$

in units of $m_e c^2$ with $F_b = B/B_{\mathrm{crit}}$ defined through Equation (66) and the characteristic energy of those pairs being $\gamma_{e,\mathrm{bh}} = r_m^{-1} K_{\mathrm{bh}} \gamma_{p,\mathrm{char}}/2$, where $r_m \equiv m_e/m_p$ is the e^- to p mass ratio and $K_{\mathrm{bh}} = 2\chi_{\mathrm{BH}}(\varepsilon_{\mathrm{bh},r}) \sim 0.25 r_m$ is numerically calculated from Equation (83).

The proton synchrotron has the peak energy of

$$\varepsilon_{\mathrm{psyn,pk}} = r_m F_b \gamma_{p,\mathrm{char}}^2 \tag{24}$$

in units of $m_e c^2$. The injection rate of the energy density of proton-synchrotron photons is

$$\dot{u}_{\mathrm{psyn}} = \frac{4}{3} r_m^3 c\sigma_T u_b \gamma_{p,\mathrm{char}}^2 f_p(\gamma_{p,\mathrm{char}}) m_p c^2. \tag{25}$$

Substituting f_p with the expression from Equation (17), we get

$$f_{\mathrm{psyn}}(\varepsilon_{\mathrm{psyn,pk}}) = \frac{4}{3} r_m u_b F_b^{-1} K_{p\gamma}^{-1} K_{\pi\to e}^{-1} \frac{\sigma_T}{\sigma_{p\gamma}} \frac{\varepsilon_2}{E_{p,\mathrm{char}}} \frac{f_{\mathrm{ph}}(\varepsilon_2)}{f_{\mathrm{ph}}(\varepsilon_{p\gamma,t})}. \tag{26}$$

Since the scattering is mainly in the Thomson regime (Equation (6)), the Y_{ssc} parameter is estimated from the energy density ratio of the low-energy photons to the magnetic field,

$$Y_{\mathrm{ssc}} \approx u_{\mathrm{phot}}/u_b \approx \varepsilon_1 f_{\mathrm{ph}}(\varepsilon_1)/u_b. \tag{27}$$

The constraints for Figure 1 are then calculated from the following equations: 1: Equation (26); 2: Equation (27); 3: Equation (18); and 4: Equation (22).

Appendix B
Kinematic Equations

We simulate time-dependent particle spectra for the above particle species. The kinematics of these particles are described by the following set of coupled integro-differential equations:

$$\partial_t n(\gamma, t) = -\partial_\gamma \{\dot{\gamma}(\gamma, t) n(\gamma, t) - \partial_\gamma [D(\gamma, t) n(\gamma, t)]/2\} - \alpha(\gamma, t) n(\gamma, t) + Q(\gamma, t), \tag{28}$$

where $n(\gamma, t)$ is the differential number density of the particle and the total number of particles equals $N = \int dV \int d\gamma n(\gamma)$. γ denotes the Lorentz factor of e^+ or e^-, or the dimensionless energy of the photon $\gamma_f = E_f/m_e c^2$.

On the right-hand side of the equation, $Q(\gamma, t)$ is the source term, representing the generation and the injection rate of the particle. For the process $a + b \to c + d$, the generation rate of the particle species c can be written as an integration over the parent particle population b:

$$Q_c(\gamma_c) = \int R(c \leftarrow b) n_b(\gamma_b) d\gamma_b, \tag{29}$$

Table 4
List of Coefficients

	Injection	Escape	Synchrotron	Inverse Compton	$\gamma\gamma \leftrightarrow e^{\pm}$	Bethe–Heitler	$p\gamma$
e^-	$Q_{e,\mathrm{inj}}$	$\alpha_{e,\mathrm{esc}}$	$\dot{\gamma}_{e,\mathrm{syn}}, D_{e,\mathrm{syn}}$	$\dot{\gamma}_{e,\mathrm{IC}}, D_{e,\mathrm{IC}}, \alpha_{e,\mathrm{IC}}, Q_{e,\mathrm{IC}}$	$\alpha_{e,\mathrm{pa}}, Q_{e,\mathrm{pp}}$	Q_{BH}	$Q_{e,p\gamma}$
e^+	...	$\alpha_{e,\mathrm{esc}}$	$\dot{\gamma}_{e,\mathrm{syn}}, D_{e,\mathrm{syn}}$	$\dot{\gamma}_{e,\mathrm{IC}}, D_{e,\mathrm{IC}}, \alpha_{e,\mathrm{IC}}, Q_{e,\mathrm{IC}}$	$\alpha_{e,\mathrm{pa}}, Q_{e,\mathrm{pp}}$	Q_{BH}	$Q_{e,p\gamma}$
γ	...	$\alpha_{f,\mathrm{esc}}$	$\alpha_{f,\mathrm{ssa}}, Q_{f,\mathrm{syn}}$	$\alpha_{f,\mathrm{IC}}, D_{f,\mathrm{IC}}$	$\alpha_{f,\mathrm{pp}}, Q_{f,\mathrm{pa}}$	$\alpha_{f,\mathrm{BH}}$	$\alpha_{f,p\gamma}, Q_{f,p\gamma}$
p	$Q_{p,\mathrm{inj}}$	$\alpha_{e,\mathrm{esc}}$	$\dot{\gamma}_{p,\mathrm{syn}}, D_{p,\mathrm{syn}}$	$\dot{\gamma}_{p,\mathrm{IC}} D_{p,\mathrm{IC}}, \alpha_{p,\mathrm{IC}}, Q_{p,\mathrm{IC}}$	...	$\dot{\gamma}_{p,\mathrm{BH}}, D_{p,\mathrm{BH}}$	$\alpha_{p,p\gamma}, Q_{p,p\gamma}$
n	...	$\alpha_{f,\mathrm{es}}$	...	...	...	...	$\alpha_{n,p\gamma}, Q_{n,p\gamma}$
ν	...	$\alpha_{f,\mathrm{es}}$	...	...	...	...	$Q_{\nu,p\gamma}$

where the integration kernel $R(c \leftarrow b)$ depends on a further layer of integration

$$R(c \leftarrow b) = \int R(c \leftarrow a, b) n_a(\gamma_a) d\gamma_a \tag{30}$$

and $R(c \leftarrow a, b)$ is the differential cross-section of generating the particle c with γ_c, averaged over the reaction angle between the incident particle a and b in the lab frame,

$$R(c \leftarrow a, b) = \frac{c}{2} \int (1 - \mu) \frac{d\sigma}{d\gamma_c d\mu} (\gamma_c, \gamma_b, \gamma_a, \mu) d\mu, \tag{31}$$

where $\mu \equiv \cos\theta$ and θ is the reaction angle between b and c.

In a process like $b + a \rightarrow b + c$, with the particle b reappearing with a different energy, the particle b on the left-hand side is nevertheless treated as "annihilated" here. The disappearance rate for b is therefore

$$\alpha(\gamma_b) = \int R(a, b) n_a(\gamma_a) d\gamma_a, \tag{32}$$

where $R(a, b)$ is

$$R(a, b) = \int R(c \leftarrow a, b) d\gamma_c, \tag{33}$$

and the b that re-appeared after the reaction is treated as a new particle. The re-appearance rate can be obtained using Equation (29).

B.1. Inverse Compton

If we consider the relativistic electrons only, i.e., $\gamma_e > 10$, the differential cross-section (expressed in units of σ_T) can be greatly simplified under the head-on collision approximation (Dermer & Menon 2009, hereafter DM09):

$$\frac{d^2\sigma_{\mathrm{IC}}}{d\gamma_{f,o} d\mu} (\gamma_{e,o}, \gamma_{e,i}, \gamma_{f,i}, \mu) = \frac{3}{8} \frac{1}{\gamma_{e,i} x^3} \left[yx^2 + 1 + 2x + \frac{1}{y}(x^2 - 2x - 2) + \frac{1}{y^2} \right] H\left(y - \frac{1}{1 + 2x} \right) H\left(1 - \frac{x}{2\gamma_{e,i}^2} - y \right), \tag{34}$$

where $x = \gamma_{e,i} \gamma_{f,i}(1 - \mu)$ is the photon energy in the electron rest frame and $y = 1 - \gamma_{f,o}/\gamma_{e,i}$. The subindex $i(o)$ stands for the incoming (outgoing) particle and $e(f)$ represents electron (photon). γ_e and γ_f are dimensionless energy units defined by $\gamma_e = E_e/m_e c^2$ and $\gamma_f = E_f/m_e c^2$,

$$R_{\mathrm{IC}}(\gamma_{f,o} \leftarrow \gamma_{e,i}, \gamma_{f,i}) = \frac{c}{2} \int (1 - \mu) \frac{d^2\sigma_{\mathrm{IC}}}{d\gamma_{f,o} d\mu} (\gamma_{e,o}, \gamma_{e,i}, \gamma_{f,i}, \mu) d\mu$$

$$= \begin{cases} \dfrac{6(1 - u)\frac{u}{v}\ln\left[\frac{u}{2v(1-u)}\right] - 3\left(\frac{u}{v} - 2 + 2u\right)\left(\frac{u}{v} + 1 + \frac{u^2}{2} - u\right)}{4v\gamma_{e,i}(u - 1)^3}, & \text{for } \dfrac{u}{2\gamma_{e,i}^2} < v < \dfrac{2u}{1 + 2u} \text{ and } u < 2\gamma_{e,i}^2 - 1/2, \\ 0 & \text{otherwise} \end{cases} \tag{35}$$

where $u = 2\gamma_{e,i}$ and $v = \gamma_{f,o}/\gamma_{e,i}$.

In the Thomson scattering limit, it reduces to

$$R_{\mathrm{IC}}(\gamma_{f,o} \leftarrow \gamma_{e,i}, \gamma_{f,i}) = \frac{\ln(w/2) - (w/2 - 1/2 - w^{-1})}{2\gamma_{f,o}/3}, \tag{36}$$

where $w = u/v = 2\gamma_{e,i}^2 \gamma_{f,i}/\gamma_{f,o}$.

The total reaction rate, averaged over the angle μ, is

$$R_{\rm IC}(\gamma_{f,i},\,\gamma_{e,i}) = \int R_{\rm IC}(\gamma_{f,o} \leftarrow \gamma_{e,i},\,\gamma_{f,i})d\gamma_{f,o}$$

$$= \frac{3c}{8u^3(1+2u)}[-2u(4+9u+u^2)+(4+u)(1+2u)^2\ln(1+2u)+4u(1+2u){\rm Li}(2,-2u)], \tag{37}$$

which has the asymptotic forms

$$R_{\rm IC}(\gamma_{f,i},\,\gamma_{e,i}) = \begin{cases} c\left(1-\dfrac{4u}{3}\right), & \text{for } u \ll 1\,(\text{Thomson}) \\[2mm] c\dfrac{3}{4u}\left[\ln\left(\dfrac{u}{2}\right)-\dfrac{1}{2}\right], & \text{for } u \gg 1\,(\text{Klein--Nishina}) \end{cases}. \tag{38}$$

${\rm Li}(2,\,x)$ is the dilogarithm defined as

$$\mathrm{Li}(2,\,z) = -\int_0^z \frac{\ln(1-t)}{t}dt. \tag{39}$$

In the Thomson regime, after scattering, the electron loses a tiny fraction of energy, and therefore the function $R_{\rm IC}(\gamma_{e,o} \leftarrow \gamma_{f,i}\gamma_{e,i})$ is highly peaked around $\gamma_{e,i}$, which the numerical grid is unable to resolve. Here, we use the differential terms to account for this effect in the numerical computation, up to the second order (VP09):

$$-\partial_\gamma\{\dot\gamma_{\rm IC}n(\gamma_e,t)-\partial_\gamma[D_{\rm IC}(\gamma_e,t)n(\gamma_e,t)]\} = -\alpha_{\rm IC}(\gamma_e,t)n(\gamma_e,t)+Q_{\rm IC}(\gamma_e,t). \tag{40}$$

Using the moment expansion (Equations (C11), (C12), (C18), and (C19) of VP09), they are expressed as

$$\dot\gamma_{\rm IC,e}(\gamma_e) = \int \gamma_f(\Psi_1-\Psi_0)n_f(\gamma_f)d\gamma_f\,, \tag{41}$$

$$D_{\rm IC,e}(\gamma_e) = \int \gamma_f^2(\Psi_2-2\Psi_1+\Psi_0)n_f(\gamma_f)d\gamma_f, \tag{42}$$

where these moments are given by Nagirner & Poutanen (1994),

$$\Psi_0(\gamma_f,\gamma_e) \approx 1-\frac{2}{3}(4\gamma_e^2-1)\gamma_f\gamma_e^{-1}+\frac{26}{5}(2\gamma_e^2-1)\gamma_f^2$$

$$\Psi_1(\gamma_f,\gamma_e) \approx \frac{1}{3}(4\gamma_e^2-1)-\frac{1}{5}(42\gamma_e^4-29\gamma_e^2+2)\gamma_f\gamma_e^{-1}+\frac{1}{25}(1176\gamma_e^4-1147\gamma_e^2+206)\gamma_f^2$$

$$\Psi_2(\gamma_f,\gamma_e) \approx \frac{1}{15}(42\gamma_e^4-34\gamma_e^2+7)-\frac{4}{75}(528\gamma_e^6-618\gamma_e^4+172\gamma_e^2-7)\gamma_f\gamma_e^{-1}$$

$$+\frac{1}{525}(109120\gamma_e^6-158856\gamma_e^4+63677\gamma_e^2-6066)\gamma_f^2. \tag{43}$$

B.2. Pair Production and Annihilation

For the pair production process, $\gamma_{f,1}+\gamma_{f,2} \rightarrow \gamma_{e,1}+\gamma_{e,2}$, two photons with dimensionless energies $\gamma_{f,i}=E_{f,i}/m_ec^2$, $(i=1,2)$ are annihilated and an electron−positron pair is produced with Lorentz factors $\gamma_{e,1}$, $\gamma_{e,2}$, respectively. Obviously, for energy conservation, we have $\gamma_{f,1}+\gamma_{f,2}=\gamma_{e,1}+\gamma_{e,2}$. We use the treatment and expressions from VP09:

$$Q_{\rm pp}(\gamma_{e,1}) = c\int_{\gamma_{f,1}^*}^\infty n(\gamma_{f,1})d\gamma_{f,1}\int_{\gamma_{f,2}^*}^\infty R_{\rm pp}(\gamma_{e,1}\leftarrow\gamma_{f,1},\gamma_{f,2})n(\gamma_{f,2})d\gamma_{f,2} \tag{44}$$

where

$$R_{\rm pp}(\gamma_{e,1}\leftarrow\gamma_{f,1},\gamma_{f,2}) = -\gamma_{f,1}^{-2}\gamma_{f,2}^{-2}[S(\gamma_{e,1},\gamma_{f,2},\gamma_{f,1},w_U)-S(\gamma_{e,1},\gamma_{f,2},\gamma_{f,1},w_L)]/4, \tag{45}$$

in which

$$S(\gamma_{e,1},\gamma_{f,2},\gamma_{f,1},w) = -[(\gamma_{f,1}+\gamma_{f,2})^2-4w^2]^{1/2}+T(\gamma_{e,1},\gamma_{f,2},\gamma_{f,1},w)+T(\gamma_{e,1},\gamma_{f,1},\gamma_{f,2},w), \tag{46}$$

where

$$T(x,y,z,w) = w^3(yz)^{-3/2}(yz-1)h^{-1}[A_0(h)-(1+h)^{1/2}]-(1+h)^{1/2}w^{-1}(yz)^{-1/2}$$

$$+(w/2)(yz)^{-3/2}[(1+h)^{-1/2}(y^2+yz+xz-xy-2w^2)-4yzA_0(h)], \tag{47}$$

where

$$A_0(h) \begin{cases} = h^{-1/2} \ln\left[h^{1/2} + (1+h)^{1/2}\right] & \text{for } h > 0 \\ = (-h)^{-1/2} \arcsin\sqrt{-h} & \text{for } h < 0, \\ \approx 1 - h/6 + 3h^2/40 & \text{for } h \approx 0 \end{cases} \tag{48}$$

and finally, with $h = [(x-y)^2 - 1]w^2/yz$ and the integration boundaries $w_L = w_-$, $w_U = \min\left[\sqrt{\gamma_{f,1}\gamma_{f,2}}, w_+\right]$, in which

$$w_\pm = \left[\gamma_{e,1}\gamma_{e,2} + 1 \pm \sqrt{(\gamma_{e,1}^2 + 1)(\gamma_{e,2}^2 + 1)}\right]/2. \tag{49}$$

The emergence rate for photons, due to the pair annihilation process, is

$$Q_{\mathrm{pa}}(\gamma_{f,1}) = c \int_{\gamma_{e,2}^*}^{\infty} n(\gamma_{e,2}) d\gamma_{e,2} \int_{\gamma_{e,1}^*}^{\infty} n(\gamma_{e,1}) R_{\mathrm{pa}}(\gamma_{f,1} \leftarrow \gamma_{e,1}, \gamma_{e,2}). \tag{50}$$

The expression for R_{pa} can be obtained via the symmetry

$$R_{\mathrm{pa}}(\gamma_{f,1} \leftarrow \gamma_{e,1}, \gamma_{e,2}) = R_{\mathrm{pa}}(\gamma_{f,2} \leftarrow \gamma_{e,1}, \gamma_{e,2}) = R_{\mathrm{pp}}(\gamma_{e,1} \leftarrow \gamma_{f,1}, \gamma_{f,2}) = R_{\mathrm{pp}}(\gamma_{e,2} \leftarrow \gamma_{f,1}, \gamma_{f,2}) \tag{51}$$

and energy conservation

$$\gamma_{f,1} + \gamma_{f,2} = \gamma_{e,1} + \gamma_{e,2}. \tag{52}$$

The lower limits of the integration in Equation (44) are

$$\gamma_{f,1}^* = \frac{1}{2}\gamma_{e,1}(1 - \beta_{e,1})$$

$$\gamma_{f,2}^* = \begin{cases} \gamma_{f,2}/\{[2\gamma_{f,2} - \gamma_{e,1}(1 + \beta_{e,1})]\gamma_{e,1}(1 + \beta_{e,1})\} & \text{for } x > x_+ \\ \gamma_{f,2}/\{[2\gamma_{f,2} - \gamma_{e,1}(1 - \beta_{e,1})]\gamma_{e,1}(1 - \beta_{e,1})\} & \text{for } x < x_- \\ \gamma_{e,1} - \gamma_{f,2} + 1 & \text{for } x_- \leqslant x \leqslant x_+ \end{cases} \tag{53}$$

with $x_\pm = [1 + \gamma_{e,1}(1 \pm \beta_{e,1})]/2$, while the limits in Equation (50) are

$$\gamma_{e,2}^* = \begin{cases} \gamma_A & \text{for } \gamma_{f,2} < 1/2 \\ 1 & \text{for } \gamma_{f,2} \geqslant 1/2 \end{cases} \qquad \gamma_{e,1}^* = \begin{cases} \gamma_- & \text{for } \gamma_{f,2} \leqslant 1/2 \\ \gamma_- & \text{for } 1/2 < \gamma_{f,2} < 1 \text{ and } \gamma_+ < \gamma_B \\ \gamma_+ & \text{for } \gamma_{f,2} \geqslant 1 \text{ and } \gamma_+ < \gamma_B \\ 1 & \text{otherwise} \end{cases}, \tag{54}$$

where

$$\gamma_\pm = (F_\pm + F_\pm^{-1})/2, \quad F_\pm = 2\gamma_{f,2} - \gamma_{e,2}(1 \pm \beta_{e,2}), \quad \gamma_A = \gamma_{f,2} + 1/(4\gamma_{f,2}), \quad \gamma_B = \gamma_{f,2} - (\gamma_{f,2} - 1)/(2\gamma_{f,2} - 1). \tag{55}$$

The disappearance rate for photons $\gamma_{f,2}$ due to pair production with a target photon $\gamma_{f,1}$ is

$$\alpha_{\mathrm{pp}}(\gamma_{f,2}) = \int R_{\mathrm{pp}}(\gamma_{f,2}, \gamma_{f,1}) n(\gamma_{f,1}) d\gamma_{f,1}, \tag{56}$$

and R_{pp} (in units of σ_T) is given by (see also DM09)

$$R(\gamma_{f,2}, \gamma_{f,1}) = \frac{3}{8} c \gamma_{f,2}^{-2} \gamma_{f,1}^{-2} \bar{\varphi}(u, v) \tag{57}$$

and

$$\bar{\varphi}(u, v) = [2v + (1+v)^{-1}]\ln u - \ln^2 u - 2(2v+1)v^{1/2}(v+1)^{-1/2} + 4\ln u \ln(1+u) + \pi^2/3 + 4\mathrm{Li}_2(-u), \tag{58}$$

where

$$v = \gamma_{f,2}\gamma_{f,1} - 1, \quad u = \frac{\sqrt{v+1} + \sqrt{v}}{\sqrt{v+1} - \sqrt{v}}. \tag{59}$$

The asymptotic form of Equation (58) is

$$\bar{\varphi}(u, v) \approx \begin{cases} 2v \ln(4v) - 4v + \ln^2(4v) & \text{for } v \gg 1 \\ \dfrac{4}{3}v^{3/2} & \text{for } v \ll 1 \end{cases}. \tag{60}$$

The pair annihilation rate is

$$\alpha_{\mathrm{pa}}(\gamma_{e,2}) = \int R_{\mathrm{pa}}(\gamma_{e,1}, \gamma_{e,2}) n(\gamma_{e,1}) d\gamma_{e,1}, \tag{61}$$

where the kernel, in units of σ_T, is

$$R_{\mathrm{pa}}(\gamma_{e,1}, \gamma_{e,2}) = \frac{3}{8} c \gamma_{e,1}^{-2} \gamma_{e,2}^{-2} [S_{\mathrm{pa}}(\gamma_e^+) - S_{\mathrm{pa}}(\gamma_e^-)], \tag{62}$$

$$S_{\mathrm{pa}}(x) = x^2 \ln(4x^2) - 2x^2 + \frac{3}{4} \ln^2(4x^2), \tag{63}$$

and

$$\gamma_e^{\pm} = \frac{1}{2}[\gamma_{e,1}\gamma_{e,2} + 1 \pm \sqrt{(\gamma_{e,1}^2 - 1)(\gamma_{e,2}^2 - 1)}]. \tag{64}$$

B.3. Synchrotron

The emission rate of synchrotron photons by a relativistic electron $\gamma_e \gtrsim 10$ is given by

$$Q_{\mathrm{syn}}(\gamma_f) = \int R_{\mathrm{syn}}(\gamma_f \leftarrow \gamma_e) n(\gamma_e) d\gamma_e. \tag{65}$$

The integration kernel is well known as

$$R_{\mathrm{syn}}(\gamma_f \leftarrow \gamma_e) = c\sigma_T(3\sqrt{3}/\pi)\gamma_f^{-1}u_b F_b^{-1}z^2 \{K_{4/3}(z)K_{1/3}(z) - (3/5)z[K_{4/3}^2(z) - K_{1/3}^2(z)]\}, \tag{66}$$

where

$$u_b = B^2/(8\pi m_e c^2), \quad F_b = B/B_{\mathrm{crit}}, \quad B_{\mathrm{crit}} = (m_e c^2)^2/(ce\hbar) = 4.41 \times 10^{13}\,\mathrm{G}, \quad z = \gamma_f \gamma_e^{-2} F_b^{-1}/3, \tag{67}$$

and $K_n(z)$ is the modified Bessel function of the second kind.

For the extinction rate of the photons due to the synchrotron-self-absorption effect, we follow the treatment of VP09:

$$\alpha_{\mathrm{ssa}}(\gamma_f) = \frac{\lambda_C^3}{8\pi} \int \gamma_f^{-1} R_{\mathrm{syn}}(\gamma_f \leftarrow \gamma_e) \gamma_e^2 \partial_\gamma [\gamma_e^{-2} n(\gamma_e)] d\gamma_e, \tag{68}$$

where $\lambda_C = h/m_e c$ is the Compton wavelength. The cooling effect on electrons, positrons, and protons, due to synchrotron and synchrotron-self-absorption effects, is modeled as a continuous energy-loss process and thus described by the differential terms

$$\dot{\gamma}_{\mathrm{syn}}(\gamma) = \dot{\gamma}_s(\gamma) + 2\gamma^{-1}H_s(\gamma) + \partial_\gamma H_s(\gamma), \quad D_{\mathrm{syn}}(\gamma) = 2H_s(\gamma), \tag{69}$$

and

$$\dot{\gamma}_s = -\frac{4}{3}\sigma_T u_B \gamma_e^2, \tag{70}$$

$$H_s(\gamma_e) = \frac{\lambda_C^3}{8\pi} \int R_{\mathrm{syn}}(\gamma_f \leftarrow \gamma_e) n(\gamma_f) d\gamma_f. \tag{71}$$

B.4. $p\gamma$ Interaction

For the $p\gamma$ interaction $p + f \to X$, with p being a proton here, f the target photon, and X representing a proton, neutron, or pion, we follow the simplified treatment *sim A* in H10, and incorporate them in this numerical framework. The generation rate of particle X can be expressed as

$$Q_X(E_X) = \int n_f(E_f) R_{p\gamma}(E_X \leftarrow E_f) dE_f, \tag{72}$$

where $Q \equiv d\dot{n}_X/dE_X$ and $n \equiv d^2N/dVdE$ so that the phenomenological values in the references can be directly applied.

The response function $R_{p\gamma}(E_X \leftarrow E_f)$ depends on a further layer of integration:

$$R_{p\gamma}(E_X) = \int R_{p\gamma}(E_X \leftarrow E_p, E_f) n_p(E_p) dE_p, \tag{73}$$

where the integration kernel is

$$R_{p\gamma}(E_X \leftarrow E_p, E_f) = cE_p^{-1} \sum_i \delta(x - \chi_i) M_i f_i(y), \tag{74}$$

where i stands for the interaction channel, M_i is the multiplicity of the particle X, χ_i is the inelasticity of the collision, $f(y)$ is defined as an integration over the cross-section as a function of photon energy ϵ_r expressed in the particle rest frame,

$$f(y) = \frac{1}{2y^2} \int_{\epsilon_{th}}^{2y} d\epsilon_r \epsilon_r \sigma(\epsilon_r), \tag{75}$$

and finally, with $x = E_X/E_p$ and $y = \gamma_p E_f$.

Under the δ-function approximation, $R_{p\gamma}(E_X \leftarrow E_f)$ simplifies to

$$R_{p\gamma}(E_X \leftarrow E_f) = c \sum_i E_{p,0}^{-1} \chi_i^{-2} E_X M_i f_i(y_0) n_p(E_{p,0}), \tag{76}$$

where $E_{p,0}$ and y_0 corresponds to the solution of $x - \chi_i = 0$. The expression for Q_X simplifies to

$$Q_X(E_X) = cn_p(\chi_i^{-1} E_X) E_X^{-1} m_p \sum_i M_i \int n_f(E_X^{-1} \chi_i m_p y) f_i(y) dy. \tag{77}$$

The disappearance rate, due to participation in the $p\gamma$ process for protons, is

$$\alpha_{p\gamma}(E_p) = \int dE_X R_{p\gamma}(E_X \leftarrow E_p) = \int dE_X \int dE_f R_{p\gamma}(E_X \leftarrow E_p, E_f) n_f(E_f) = c \sum_i M_i \int dE_f n_f(E_f) f_i(\gamma_p E_f), \tag{78}$$

and for photons,

$$\alpha_{p\gamma}(E_f) = \int dE_X R_{p\gamma}(E_X \leftarrow E_f) = c \sum_i \chi_i^{-1} M_i \int dE_X f_i(\chi_i^{-1} E_X E_f m_p^{-1}) n_p(\chi_i^{-1} E_X). \tag{79}$$

The expressions of $f_i(y)$ and coefficients are given by Equations (30), (33)–(35), and (40) and Tables 3, 5, 6 of HU10 when i falls into the categories of resonance, direct, and multi-pion production, respectively.

B.5. Bethe–Heitler

For the BH or photo-pair process $p + \gamma_f \rightarrow \gamma_{e,1} + \gamma_{e,2}$, we incorporate the calculation using the framework similar to the multi-pion production in the previous section. The generation rate for pairs is given by Equation (77), where the multiplicity $M = 1$ for e^- and e^+, respectively. The cross-section and inelasticity are approximated by a series of step functions, where each step is defined as an interaction channel i. The cross-section $\sigma_{BH}(\gamma'_f)$ as a function of photon energy (in units of $m_e c^2$) γ'_f in the proton rest frame, obtained under the approximation of zero recoil of the proton, can be expressed as

$$\sigma_{BH,tot}(\gamma'_f) = \int_1^{\gamma'_f} d\gamma_{e,1} \int_{-1}^{+1} d\mu_{e,1} \frac{d^2\sigma_{BH,diff}}{d\gamma_{e,1} d\mu_{e,1}}, \tag{80}$$

where the differential cross-section in the proton rest frame is expressed as (Blumenthal 1970):

$$\frac{d^2\sigma_{BH,diff}}{d\gamma_{e,1} d\mu_{e,1}} = \left(\frac{3\alpha_f \sigma_T p_1 p_2}{16\pi\gamma_f^3}\right)\left[-4(1-\mu^2)\frac{2\gamma_1^2+1}{p_1^2\Delta_1^4} + \frac{5\gamma_1^2 - 2\gamma_1\gamma_2 + 3}{p_1^2\Delta_1^2} + \frac{p_1^2 - \gamma_f^2}{T^2\Delta_1^2} + \frac{2\gamma_2}{p_1^2\Delta_1} + \frac{Y}{p_1 p_2}\left(2\gamma_1(1-\mu^2)\right.\right.$$
$$\times \frac{3\gamma_f + p_1^2\gamma_2}{\Delta_1^4} + \frac{2\gamma_1^2(\gamma_1^2 + \gamma_2^2) - 7\gamma_1^2 - 3\gamma_1\gamma_2 - \gamma_2^2 + 1}{\Delta_1^2} + \left.\frac{\gamma_f(\gamma_1^2 - \gamma_1\gamma_2 - 1)}{\Delta_1}\right)$$
$$\left. - \frac{\delta_+^T}{p_2 T}\left(\frac{2}{\Delta_1^2} - \frac{3\gamma_f}{\Delta_1} - \frac{\gamma_f(p_1^2 - \gamma_f^2)}{T^2\Delta_1}\right) - \frac{2y_+}{\Delta_1}\right], \tag{81}$$

where

$$T=|\mathbf{k} - \mathbf{p}_1|, \quad Y = \frac{2}{p_1^2} \ln\left[\frac{\gamma_1\gamma_2 + p_1 p_2 + 1}{\gamma_f}\right], \quad y_+ = p_2^{-1}\ln\left[\frac{\gamma_2 + p_2}{\gamma_2 - p_2}\right], \quad \delta_+^T = \ln\left[\frac{T + p_2}{T - p_2}\right], \quad \Delta_1 = \gamma_1(1 - \beta_1\mu), \tag{82}$$

and in the above equations we have dropped the primes and the electron subindex e (in which, $1 = e^-$, $2 = e^+$).

The inelasticity for one electron can be obtained via

$$\chi_{\mathrm{BH}}(\gamma_f) = \frac{m_e}{m_p} \int_1^{\gamma_f - 1} d\gamma_1 \int_{-1}^{+1} d\mu \Delta_1 \frac{d^2\sigma_{\mathrm{BH,diff}}}{d\gamma_1 d\mu}. \tag{83}$$

Equations (80) and (83) are approximated as a sum of step functions:

$$\sigma_{\mathrm{BH,tot}}(\gamma_f) = \sum_i \sigma_{\mathrm{BH},i,0} H(\gamma_f - \gamma_{f,i}^{\min}) H(\gamma_{f,i}^{\max} - \gamma_f)$$

$$\chi_{\mathrm{BH}}(\gamma_f) = \sum_i \chi_{\mathrm{BH},i,0} H(\gamma_f - \gamma_{f,i}^{\min}) H(\gamma_{f,i}^{\max} - \gamma_f), \tag{84}$$

where

$$\sigma_{\mathrm{BH},i,0}(\gamma_f) = \frac{1}{\gamma_{f,i}^{\max} - \gamma_{f,i}^{\min}} \int_{\gamma_{f,i}^{\min}}^{\gamma_{f,i}^{\max}} d\gamma_f \, \sigma_{\mathrm{BH,tot}}(\gamma_f)$$

$$\chi_{\mathrm{BH},i,0}(\gamma_f) = \frac{1}{\gamma_{f,i}^{\max} - \gamma_{f,i}^{\min}} \int_{\gamma_{f,i}^{\min}}^{\gamma_{f,i}^{\max}} d\gamma_f \, \chi_{\mathrm{BH}}(\gamma_f), \tag{85}$$

and the functions $\{f_{\mathrm{BH},i}(y)\}$ are obtained from Equation (40) of HU10 by replacing the coefficients with the ones from the above equation.

The extinction function of the photons is

$$\alpha_{\mathrm{BH}}(\gamma_f) = 2c \sum_i \chi_{\mathrm{BH},i,0}^{-1} \int dE_1 f_{\mathrm{BH},i}(\chi_{\mathrm{BH},i,0}^{-1} E_1 E_f m_p^{-1}) \, n_p(\chi_{\mathrm{BH},i,0}^{-1} E_1). \tag{86}$$

For protons, the generation rate in principle can be obtained from Equation (77) by substituting $M_i = 1$, $f_i = f_{\mathrm{BH},i}$, and $\chi_i = 1 - 2\chi_{\mathrm{BH},i,0}$. However, since $\chi_{\mathrm{BH},i,0} \ll 1$, $\chi_i \approx 1$, the term $n_p(\chi_i^{-1} E_p)$ almost overlaps with the parent proton bin $n_p(E_p)$, and the numerical grid cannot resolve this difference. Instead, similar to the case of IC scattering in the Thomson regime, this effect is treated as a continuous energy-loss process and thus described by the differential terms. By requiring equality between the integral terms and the differential terms, such as Equation (40), we have

$$\dot{E}_{\mathrm{BH}}(E_p) = \sum_i - 2\chi_{\mathrm{BH},i,0} E_p \alpha_{p,i}(E_p)$$

$$D_{\mathrm{BH}}(E_p) = \sum_i 4\chi_{\mathrm{BH}}^2 E_p^2 \alpha_{p,i}(E_p), \tag{87}$$

where we have defined $\alpha_{p,i}(E_p) = 2c \int dE_f n_f(E_f) f_{\mathrm{BH},i}(\gamma_p E_f)$.

B.6. π Decay Kinematics

The dominant decay channels of $\pi^\pm$ and $\mu^\pm$ are

$$\pi^+(\pi^-) \to \mu^+(\mu^-) + \nu_\mu(\bar{\nu}_\mu)$$

$$\mu^+(\mu^-) \to e^+(e^-) + \nu_e(\bar{\nu}_e) + \bar{\nu}_\mu(\nu_\mu). \tag{88}$$

The probability density function for the decay product j from the parent particle i, as a function of scaling variable $x = E_j/E_i$, is (Lipari et al. 2007)

$$f_{\mu_R^+}(x) = f_{\mu_L^-}(x) = \frac{r_{\mu\pi}^2(1 - x)}{(1 - r_{\mu\pi}^2)^2 x} H(x - r_{\mu\pi}^2)$$

$$f_{\mu_L^+}(x) = f_{\mu_R^-}(x) = \frac{x - r_{\mu\pi}^2}{(1 - r_{\mu\pi}^2)^2 x} H(x - r_{\mu\pi}^2). \tag{89}$$

Due to energy conservation, the corresponding neutrino directly from pion decay has a distribution function of

$$f_\nu(1 - x) = f_\mu(x). \tag{90}$$

17

For $\pi^0 \rightarrow \gamma + \gamma$, the distribution function for a photon is

$$f_\gamma(x) = \frac{1}{2\beta_\pi \gamma_\pi} H\left(x - \frac{1 - \beta_\pi}{2}\right) H\left(\frac{1 + \beta_\pi}{2} - x\right). \tag{91}$$

The neutrino distribution function from muon decay is

$$f_{\bar{\nu}_\mu}(x, h) = f_{\nu_\mu}(x, -h) = \left(\frac{5}{3} - 3x^2 + \frac{4}{3}x^3\right) + h \times \left(-\frac{1}{3} + 3x^2 - \frac{8}{3}x^3\right)$$

$$f_{\nu_e}(x, h) = f_{\bar{\nu}_e}(x, -h) = (2 - 6x^2 + 4x^3) + h \times (2 - 12x + 18x^2 - 8x^3), \tag{92}$$

and for $e^\pm$, since we no longer need to distinguish between their chiralities in this paper, the distribution can be simply expressed as (e.g., Particle Data Group)

$$f_e(x) = \frac{4}{3}(1 - x^3) \tag{93}$$

under the relativistic approximation, $\gamma_e \gtrsim 10$.

Appendix C
Numerical Treatment

For the numerical aspect, it is more convenient to rewrite Equation (28) in the form where energy is expressed on the logarithmic scale,

$$\partial_t n(x, t) = -\partial_x[A(x, t)n(x, t) - B(x, t)\partial_x n(x, t)] - \alpha(x, t)n(x, t) + \epsilon(x, t), \tag{94}$$

by making the substitutes

$$x = \ln\gamma, \ n(x) = \gamma n(\gamma), \ A(x) = \frac{\dot{\gamma}}{\gamma} - \partial_\gamma\left[\frac{D(\gamma)}{2\gamma}\right], \ B(x) = \frac{D(\gamma)}{2\gamma}, \ \epsilon(x) = \gamma Q(\gamma), \ \alpha(x) = \alpha(\gamma), \tag{95}$$

where the terms on the right-hand sides are the ones from Equation (28) while the left-hand sides correspond to Equation (94).

The x-axis is equally spaced with width of Δx from $x_{\min}$ to $x_{\max}$, which represents energy on the logarithmic scale,

$$n_i = n_{\min} + (i - 1)\Delta x, \ i = 1, 2, \ldots i_{\max}, \tag{96}$$

and t-axis is linear in time, and equally spaced with width of Δt,

$$n^k = n^0 + (k - 1)\Delta t, \ k = 1, 2, \ldots t_{\max}. \tag{97}$$

The discrete form of Equation (94) can be written, with the abbreviated notations here on the index of any quantity s:

$$s \equiv s_i^k, \ s_1 \equiv s_{i+1}, \ s_{-1} \equiv s_{i-1}, \ s^1 \equiv s^{k+1}, \text{ etc.} \tag{98}$$

as

$$(n^1 - n)/\Delta t = -(F_+^+ - F_-^+)/\Delta x - \alpha \times (n^1 - n) + \epsilon, \tag{99}$$

where

$$F_\pm^+ = A_\pm n_\pm^+ - B_\pm(n_\pm^+ - n^+)/\Delta x. \tag{100}$$

The differential scheme on time is Crank–Nicolson, which is

$$n^+ = (n^1 + n)/2, \tag{101}$$

and on energy is Chang & Cooper (Chang & Cooper 1970), which is

$$n_+ = (1 - \delta)n_1 + \delta * n, \tag{102}$$

where

$$\delta = \frac{1}{w} - \frac{1}{e^w - 1}, \ w = -\frac{A_+}{B_+}\Delta x. \tag{103}$$

At very high energies, the secondary electron or positron loses energy rapidly within a feasible choice of computational time step Δt, and this process cannot be properly calculated from the above framework. Instead, in this region, we switch to a semi-analytical approach of Equation (94) but have ignored the second-order differential term $B(x)$, which is a trade-off between a small fraction of accuracy and orders-of-magnitude increase in efficiency. Since in this region the cooling coefficient $A(x)$ is mainly contributed by

low-energy target photons and the magnetic field, with a proper choice of Δt and partition of this region, (1) $A(x)$ can be treated as a constant within each Δt; and (2) the time-dependent solution in each energy bin quickly converges to a steady-state solution within Δt. Therefore, semi-analytical solutions can be obtained and represented for the electron and positron populations for each time step Δt by the following:

$$n(x, t + \Delta t) = \frac{A(y, t)}{A(x, t)} \exp\left[-\int_y^x \frac{\alpha(x', t)}{A(x', t)} dx'\right] n(y, t) + \frac{1}{A(x, t)} \int_y^x dx' \epsilon(x', t) \exp\left[-\int_{x'}^x \frac{\alpha(x'', t)}{A(x'', t)} dx''\right], \quad (104)$$

where y is the solution of the equation

$$-\int_1^y \frac{dx'}{A(x', t)} = -\int_1^x \frac{dx'}{A(x', t)} + \Delta t, \quad (105)$$

which can be easily calculated numerically.

References

Aartsen, M. G., Abbasi, R., Abdou, Y., et al. 2013, PhRvL, 111, 021103
Aartsen, M. G., Abraham, K., Ackermann, M., et al. 2017, ApJ, 835, 45
Aartsen, M. G., Ackermann, M., Adams, J., et al. 2015, ApJL, 805, L5
Abbasi, R., Abdou, Y., Abu-Zayyad, T., et al. 2012, Natur, 484, 351
Ahlers, M., & Halzen, F. 2014, PhRvD, 90, 043005
Ajello, M., Gasparrini, D., Sánchez-Conde, M., et al. 2015, ApJL, 800, L27
Bechtol, K., Ahlers, M., Di Mauro, M., Ajello, M., & Vandenbroucke, J. 2017, ApJ, 836, 47
Becker Tjus, J., Eichmann, B., Halzen, F., Kheirandish, A., & Saba, S. M. 2014, PhRvD, 89, 123005
Blumenthal, G. R. 1970, PhRvD, 1, 1596
Böttcher, M., Reimer, A., Sweeney, K., & Prakash, A. 2013, ApJ, 768, 54
Bromberg, O., & Levinson, A. 2009, ApJ, 699, 1274
Chang, J. S., & Cooper, G. 1970, JCoPh, 6, 1
Chen, X., Pohl, M., & Böttcher, M. 2015, MNRAS, 447, 530
Chen, X., Pohl, M., Böttcher, M., & Gao, S. 2016, MNRAS, 458, 3260
Dermer, C. D., & Menon, G. 2009, High Energy Radiation from Black Holes: Gamma Rays, Cosmic Rays, and Neutrinos (Princeton, NJ: Princeton Univ. Press)
Dermer, C. D., Murase, K., & Inoue, Y. 2014, JHEAp, 3, 29
Diltz, C., & Böttcher, M. 2016, ApJ, 826, 54
Diltz, C., Böttcher, M., & Fossati, G. 2015, ApJ, 802, 133
Dimitrakoudis, S., Petropoulou, M., & Mastichiadis, A. 2014, APh, 54, 61
Eichmann, B., Schlickeiser, R., & Rhode, W. 2012, ApJ, 744, 153
Finke, J. D., Dermer, C. D., & Böttcher, M. 2008, ApJ, 686, 181

Fossati, G., Maraschi, L., Celotti, A., Comastri, A., & Ghisellini, G. 1998, MNRAS, 299, 433
Ghisellini, G., Righi, C., Costamante, L., & Tavecchio, F. 2017, MNRAS, 469, 255
Giannios, D. 2013, MNRAS, 431, 355
Giannios, D., Uzdensky, D. A., & Begelman, M. C. 2009, MNRAS, 395, L29
Halzen, F., & Kheirandish, A. 2016, ApJ, 831, 12
Hooper, D. 2016, JCAP, 9, 002
Hümmer, S., Rüger, M., Spanier, F., & Winter, W. 2010, ApJ, 721, 630
IceCube Collaboration 2013, Sci, 342, 1242856
Kadler, M., Krauß, F., Mannheim, K., et al. 2016, NatPh, 12, 807
Krauß, F., Kadler, M., Mannheim, K., et al. 2014, A&A, 566, L7
Lipari, P., Lusignoli, M., & Meloni, D. 2007, PhRvD, 75, 123005
Murase, K., Ahlers, M., & Lacki, B. C. 2013, PhRvD, 88, 121301
Murase, K., Guetta, D., & Ahlers, M. 2016, PhRvL, 116, 071101
Murase, K., Inoue, Y., & Dermer, C. D. 2014, PhRvD, 90, 023007
Nagirner, D. I., & Poutanen, J. 1994, Single Compton scattering (Amsterdam: Harwood Academic Publishers)
Padovani, P., Resconi, E., Giommi, P., Arsioli, B., & Chang, Y. L. 2016, MNRAS, 457, 3582
Petropoulou, M., Coenders, S., & Dimitrakoudis, S. 2017, APh, 80, 115
Petropoulou, M., Dimitrakoudis, S., Padovani, P., Mastichiadis, A., & Resconi, E. 2015, MNRAS, 448, 2412
Righi, C., Tavecchio, F., & Guetta, D. 2017, A&A, 598, 36
Stecker, F. W., Malkan, M. A., & Scully, S. T. 2012, ApJ, 761, 128
Tavecchio, F., Pacciani, L., Donnarumma, I., et al. 2013, MNRAS, 435, L24
Turley, C. F., Fox, D.B., Murase, K., et al. 2016, ApJ, 833, 117
Vurm, I., & Poutanen, J. 2009, ApJ, 698, 293